POLITECNICO DI MILANO

SCUOLA DI INGEGNERIA INDUSTRIALE E DELL'INFORMAZIONE

Dipartimento di Elettronica, Informazione e Bioingegneria

Tesi di Laurea in
INGEGNERIA BIOMEDICA

Radiotherapy effect assessment through diffusion weighted imaging on patients affected by prostate cancer

Relatore: Prof. Luca Mainardi
Correlatore: Ing. Eros Montin

Tesi di Laurea di:
Marta Bianchi 786676
Roberta Civita 798787

Anno Accademico 2013-2014

Contents

List of Figures

List of Tables

Abstract

This thesis has been carried out at the Analysis Laboratory Radiological Advanced, in collaboration with the Department of Electronic Information, Bioengineering (DEIB) of Politecnico di Milano and the department of Diagnostic Imaging and Radiotherapy of the Fondazione IRCCS National Cancer Institute (INT). It aims to assess the radiotherapy effects on healthy tissues, in particular within the penile bulb, of those patients that are affected with prostate cancer. The analysis has been carried out on a sample of five patients and for each protocol it provides for the acquisition of magnetic resonance imaging (MRI) before and after radiotherapy (RT), computed tomography (CT) and the dose received by the patient. The MRI images for each exam include four diffusion images at different b_value (0, 150, 800, 1000 $\frac{s}{mm^2}$), a morphological T2 pre contrast and two morphological T1 pre and post contrast. Dose images generally three for each patient and are acquired during the first exam. The apparent diffusion coefficient (ADC) is an index used to assess how the bulb has changed as a result of the radiotherapy treatment. Before comparing the ADC values in the penile bulb before and after radiation therapy, we implemented a registration method and a segmentation algorithm.
To evaluate functional variations in tissues due to RT, patients un-

derwent two MRI scans concerning morphological and functional sequences, a first one before the RT and a second one at the end of the treatment. Therefore three registrations were computed: an intra-exam fusion (between DWI and morphological T1 PRE image) and two inter-exam: one for the registration of the post-treatment on the pre-treatment and the second for the placing of the CT on the morphological PRE image. Each registration was divided in two parts. In the first one, a translation and an affine transformation were performed in order to account the macro movement of the patient during the scan; in the second part, a local non-rigid free form deformation based on b-spline was estimated. The goal of the fusion is determining the correspondence of features between moving and fixed images. In order to quantify the error committed in the registrations, we implemented three validation procedures, one for each fusion.

The second part of the current work includes a segmentation algorithm of the MR images. This section aims to develop an automatic method for the identification of penile bulb. The penile bulb is a small area within the prostate that looks like an healthy tissue marginally affected during radiotherapy treatment. Data from several image techniques were available, for this reason the procedure could be defined multidimensional. Usually, the information content inside these images is redundant. Principal Component Analysis (PCA) is the most widespread data reduction technique, used to reduce the number of dimensions in a multiple variables problem. Penile bulb identification has been performed through of a fuzzy approach. In order to segment automatically the penile bulb, we have collected typical grey levels of the speciment from multidimensional dataset. We have used different

membership functions that represent the probability of the pixels to be labelled bulb through voxel intensities and geometrical features. Sixteen probability maps, eight for the PRE scan and eight for the POST one, result by applying these membership functions as a look-up table on the PRE and POST images. For each exam, we computed a fuzzy conjunction operation by applying Mamdani minimum implication rules. At the end of this procedure we obtained two maps, one for each exam, measuring the labelling probability. In order to find the best combination of threshold and number of components, we performed a validation step. In this 3D-space (number of components, threshold value and percentage), we defined a metric to optimize both sensitivity and specificity of the technique. By maximizing this metric, we could find the optimal fuzzy set creator, threshold and number of components. We noticed that the little changes in the number of components used in the PCA or threshold result in a decrease of the sensibility and in an increase of the specificity.

The following step concerned to compute the ADC values within segmented penile bulb, before and after the radiotherapy. Each box-plots corresponds to a patient, as reported in Figure 1. The overall effect on the population was that ADC rose in the short period after the radiotherapy, although for some patients in a more evident way than in others. We noticed a greater increase in both the third and fifth patient. In order to make the patients comparable, we normalized the ADC variation, as follows:

$$normalized\ ADC\ values = \frac{post\ treatment\ ADC - pre\ treatment\ ADC}{pre\ treatment\ ADC} \tag{1}$$

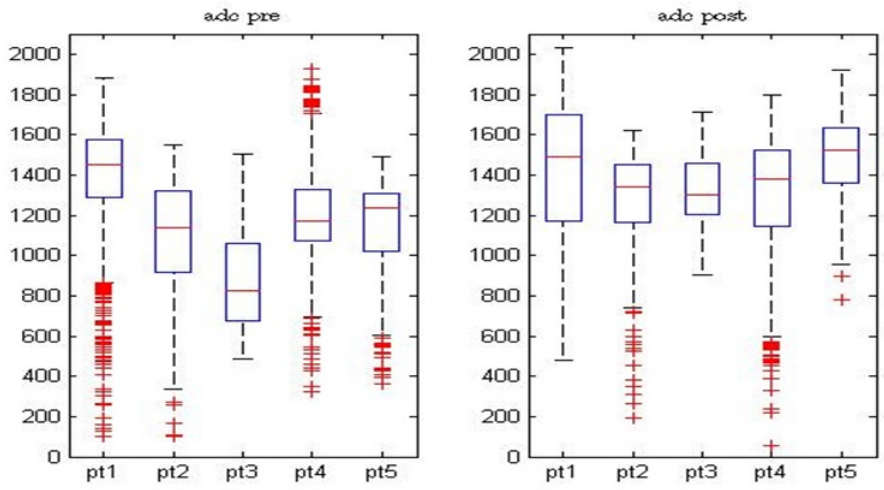

Figure 1: ADC values calculated before and after the radiotherapy treatment: the increase of the ADC values from the pre to the post treatment examination is very obvious to all patients.

Positive values mean an increase of the post-treatment ADC compared to the pre-treatment one, while negative values were the other way around. Afterwards, we represented the mean ADC and dose values for each patient, as shown in Figure 2. We observed small variations in ΔADC values for the ranges of dose considered. Therefore, a low ADC growth was not in every case justifiable with a low quantity dose. We found different increases of ADC for a comparable dose values. In order to find other elements related with the changes in the penile bulb, we examined the International Index of Erectile Functionality questionnaires (IIEF). We classified the patients into two group: the first group included individuals with a moderate or severe erectile dysfunction (patients 1 and 2); the second one consisted of the patients, who had a mild or no erectile dysfunction (patients 3, 4 and 5). Then, we compared the mean and median ADC value with the IIEF score.

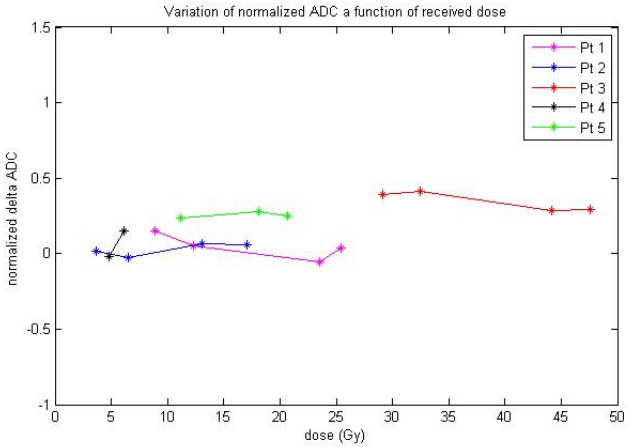

Figure 2: Variations in ΔADC values for the ranges of dose considered.

As reported in figure 3, the averages for the first group were lower than the values of the second one. The same result was found for the median ADC values. Therefore we concluded that the erectile dysfunction is uncorrelated to the RT.

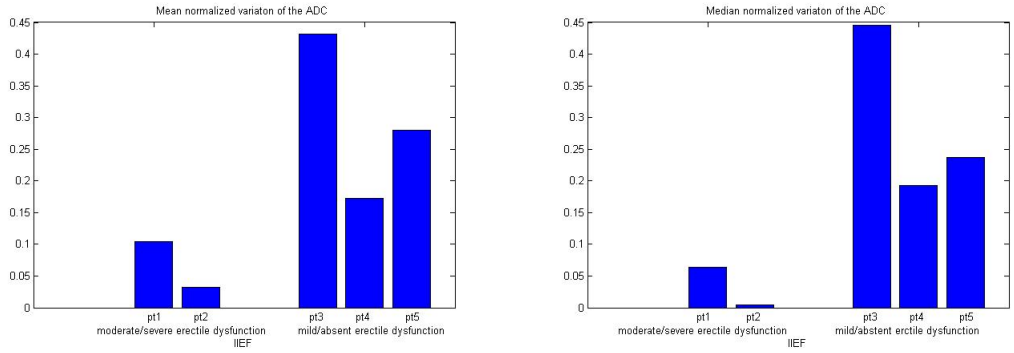

Figure 3: The outcome of the IIEF questionnaires in function of the mean or median calculated for normalized variation ADC of each patient.

Summary

Il presente lavoro di tesi magistrale é stato svolto all'interno del Laboratorio di Analisi Radiologiche Avanzate (LARA), nato da una collaborazione tra il Dipartimento di Elettronica, Informazione e Bioingegneria (DEIB) del Politecnico di Milano e il Dipartimento di Diagnostica per Immagini e Radioterapia della Fondazione IRCCS Istituto Nazionale dei Tumori (INT). Lo studio si propone di valutare gli effetti della radioterapia sui tessuti sani, in particolare sul bulbo penieno, in pazienti affetti da tumore al distretto prostatico. L'analisi é stata svolta su un campione di cinque pazienti e per ognuno il protocollo prevede l'acquisizione di immagini di risonanza magnetica (MR) prima e dopo la radioterapia, di tomografia compiuterizzata (CT) e di dose ricevuta dal soggetto. Le immagini MR, per ogni esame, comprendono quattro immagini di diffusione a diversi b_value (0, 150, 800, 1000 $\frac{s}{mm^2}$), una morfologica T2 pre contrasto, due morfologiche T1 pre e post contrasto. Le immagini di dose sono tre per ogni paziente e sono state acquisite durante il primo esame. Per valutare come il bulbo sia cambiato a seguito della radioterapia, si é considerato il coefficiente di diffusione apparente (ADC), un indice di cellularitá del tessuto che valuta il grado di diffusione molecolare ristretta dovuta alla presenza di membrane cellulari. Prima di confrontare i valori di ADC in cor-

rispondenza del bulbo prima e dopo la radioterapia, é stato necessario implementare una procedura di registrazione delle immagini e sviluppare un algoritmo di segmentazione.
I pazienti vengono sottosposti a due esami di MR, che prevedono l'acquisizione di sequenze morfologiche e funzionali. La registrazione ha lo scopo di riallineare e rimappare nello stesso spazio due immagini che si vogliono confrontare. Le registrazioni effettuate per ogni paziente sono tre: una intra-esame (tra DWI e immagine morfologica T1 del corrispondente esame) e due inter-esame (tra la morfologiche pre e post trattamento e tra CT e morfologica pre trattamento). Ogni registrazione prevede l'implementazione di una traslazione e di una trasformazione affine (al fine di risolvere gli errori di registrazione dovuti ai macro movimenti che subisce il paziente durante l'acquisione) seguiti da una trasformazione non rigida, basata sulle b-spline.
Si vogliono quindi testare, tramite una procedura di validazione, le tre registrazioni per quantificare l'errore commesso durante ciascuna implementazione.
La seconda parte di questo studio riguarda l'implementazione di una procedura di segmentazione su immagini di risonanza magnetica. Lo scopo della procedura é quello di segmentare in maniera automatica il bulbo penieno. L'area anatomica in questione si trova in prossimitá della prostata e riceve parte delle radiazioni dirette all'organo obbiettivo durante la radioterapia. Il metodo che verrá descritto puó essere definito multidimensionale in quanto verrano utilizzate immagini acquisite con tecniche diverse. Spesso l'informazione contenuta all'interno di queste immagini é rindondante. L'analisi delle componenti principali (PCA) é la tecnica di riduzione dei dati piú diffusa.

Nel presente lavoro, la segmentazione é stata eseguita attraverso un approccio fuzzy. Per implementare l'algoritmo, vengono collezionati i livelli di grigio di un campione multidimensionale di dati. Vengono utilizzate diverse *membership functions* (MFs), che rappresentano la probabilitá dei pixels di appartenere al bulbo, secondo caratteristiche geometriche e di intensitá. Applicandole al dataset iniziale, si ottengono sedici mappe di probabilitá, 8 per gli esami pre trattamento e 8 per gli esami post trattamento. Le otto mappe di probabilitá vengono quindi combinate secondo le regole di implicazioni di Mamdani. Alla fine della procedura, si ottengono due mappe, una per ogni esame, che misurano la probabilitá dei pixels di appartenere al bulbo.
Per determinare la miglior combinazione tra il numero di componenti principali e la soglia, si é voluto implementare una procedura di validazione della segmentazione. Nello spazio 3-D (numero di componenti, soglia e specificitá/sensitivitá), viene cosí definita una cifra di merito in grado di massimizzare contemporaneamente sensitivitá e specificitá. Dall'ottimizzazione di questa cifra di merito, é posssibile trovare il miglior metodo di segmentazione, in corrisponenza di una determinata soglia e componente principale. Dai risultati ottenuti, si evince che una piccola variazione nel numero di componente o soglia determina una diminuzione evidente nella specificitá e sensitivitá.
Una volta che le immagini sono state registrate e il bulbo segmentato, sono stati confrontati i valori di ADC pre e post trattamento (Figura 4). Risulta immediatamente visibile che l'ADC si sia alzato dopo il trattamento, anche se per alcuni individui in maniera piú evidente di altri. I maggiori incrementi si riscontrano nel terzo e nel quinto paziente. Per rendere comparabili le variazioni tra i diversi individui,

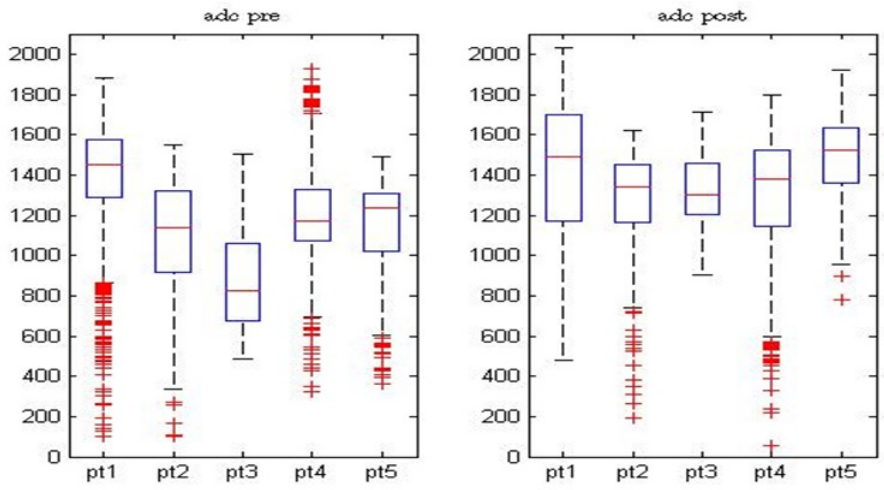

Figure 4: Valori di ADC calcolati prima e dopo la radioterapia: l'aumento di ADC é dal pre al post trattamento é molto evidente per tutti i pazienti esaminati.

abbiamo normalizzato la variazione di ADC come segue:

$$normalized\ ADC\ values = \frac{post\ treatment\ ADC - pre\ treatment\ ADC}{pre\ treatment\ ADC} \tag{2}$$

Valori positivi indicano un aumento dell'ADC post trattamento, mentre valori negativi corrispondono ad un decremento. Abbiamo quindi cercato il modo di evidenziare una possibile relazione tra questa variazione percentuale di ADC e la dose ricevuta dal paziente (Figure 5). Tre pazienti hanno avuto un incremento di ADC compreso tra lo 0% e il 6%, mentre per i rimanenti due l'incremento é stato del 35% e del 25%. I risultati mostrano che per piccole variazioni di dose all'interno del bulbo non si sono verficati grossi cambiamenti nella variazione di ADC percentuale. Questo significa che ci sono altri elementi connessi

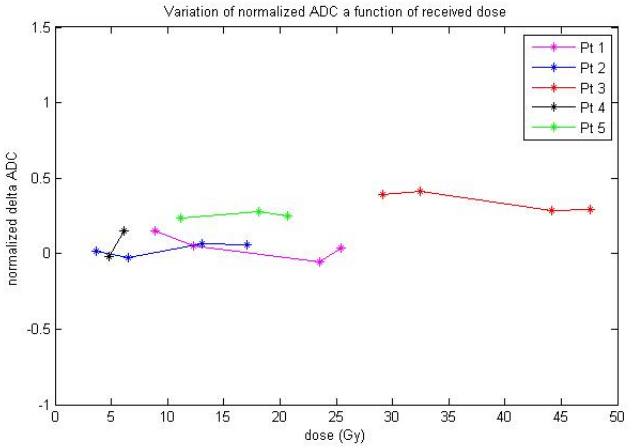

Figure 5: Piccole variazioni di dose all'interno del bulbo non corrispondono a grossi cambiamenti nel ΔADC normalizzato.

ai cambiamenti nel bulbo. Per identificarli, abbiamo esaminato i questionari IIEF, somministrati ai pazienti, che valutano la disfunzione erettile. Abbiamo classificato i pazienti in due gruppi: al primo appartenevano coloro che hanno sviluppato una disfunzione erettile grave o moderata (pazienti 1 e 2), mentre al secondo appartenevano coloro che hanno dichiarato una disfunzione minima o assente (pazienti 3, 4 e 5). Abbiamo quindi comparato i valori di ADC medi e mediani nel bulbo per i due gruppi (Figura 6). I pazienti che avevano una disfunzione erettile grave o moderata hanno subito una minor variazione di ADC. Pertanto si puó concludere che la disfunzione erettile non puó essere correlata alla RT.

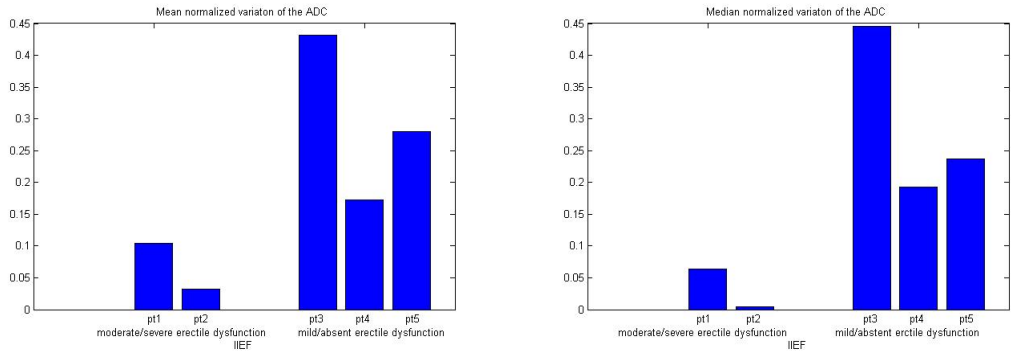

Figure 6: Esito dei questionari IIEF in funzione della media o mediana calcolata per i valori di ΔADC normalizzato di tutti i pazienti analizzati.

Introduction

The purpose of this study is to assess the functional response to radiotherapy treatment of healthy tissues, in particular the penile bulb, in patients affected by prostate cancer. Prostate cancer represents for incidence, morbidity and mortality a relevant issue for the majority of health care institutions [38] [31]. Therefore, there is an ongoing commitment from health care institution to ensure proper information on that topic and, sometimes, reassurance to both patients and their families, to health professionals and to the social community. As most solid tumours, the aetiology of prostate cancer is multi factorial [38]. It results from a complex interaction of genetic factors, which are responsible for the familiar and the different incidence of the human race, and environmental factors (i.e. dietary factors and carcinogens present in the environment). The most important casual factors have been identified as the advanced age and the presence of androgen hormones biologically active in the circulating blood and prostate tissues. Data gathered through clinical and epidemiological researches demonstrate that prostate cancer is still the second cause of death among malignant disease in both United States and European males [38] [6]. Despite this, even today there are many disputes on risks and benefits of an early diagnosis and treatments carried out in several stages of

the disease. In particular, magnetic resonance imaging (MRI) is part of the diagnostic work-up for staging and detection of these lesions [1]. Diffusion-weighted imaging (DWI) [2] is an MRI functional imaging technique which can reveal the water movement freedom in extracellular space and therefore contrast tissues alterations. Several studies enhance the growing role of DWI in the diagnosis and follow-up of the tumour. The assessment of DWI images [43] is usually performed through apparent diffusion coefficient (ADC) [4], a parameter widely recognized as an indispensable tool in the examination. As a result of recent years technological developments, nowadays it is possible to deliver accurate high-dose radiation therapy (EBRT) for patients with prostate cancer, through the application of techniques such as conformal/intensity modulated (IMRT) [3] [8] and the precise localization guided by the imaging of the prostate and critical organs that surround it. However, despite the accuracy in both the definition of the target to be irradiated and the irradiation techniques, a significant number of patients still show acute (within the three next months after the start of the therapy) and late (from six to twenty-four months) toxicity. The reason for that is due to the inevitable inclusion of portions of the organs at risk within the "planning target volume" (PTV).

Aim of thesis

The current study proposes to determine the effects of radiation at the cellular level on healthy tissues. It identifies a parameter correlated with cellularity that assess functional variations in tissues under therapy. Furthermore, this study evaluates whether the changes within the region of interest, in particular penile bulb, are related exclusively to

the dose received by the patient or also due to some other characteristics that may determine a subjective radiosensitivity. Part of the study arises from a previous work in which it has been registered the available images and then tuned-up an automatic segmentation method to identify the tissues of interest.

Chapter 1

Prostate, its pathologies and diagnostic instruments

1.1 Prostate

Embryologically, the prostate, seminal vesicles, and ducts deferens originate from two separate structures [17]. The prostate arises from a budding collection of tissue in the urogenital sinus. The seminal vesicles and the ductus deferens are formed from the mesonephric duct. The prostate develops from epithelial outgrowths form the prostatic segment of the urethra that grows into the surrounding mesenchyme. This outgrowth and branching start at week ten during embryo growth; by week twelve, there are five groups of tubules that form the lobes of the prostate. The first group makes up the middle lobe; the second and third groups make up the right and left lateral lobes; the fourth group is the posterior lobe that starts from the floor of the urethra and the fifth group is the anterior lobe.

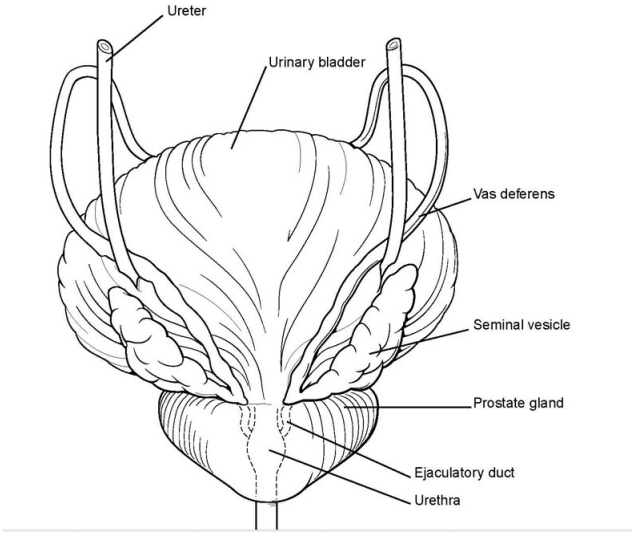

Figure 1.1: Posterior view of the prostate gland

1.1.1 Anatomy

A normal prostate gland is approximately 20 g in volume, 3 cm in length, 4 cm wide, and 2 cm in depth [33]. As men get older, the prostate gland is variable in size secondary to benign prostatic hyperplasia [6]. The gland is located posterior to the pubic symphysis, superior to the perineal membrane, inferior to the bladder, and anterior to the rectum (Figure 1.1). The base of the prostate is in continuity with the bladder and the prostate ends at the apex before becoming the striated external urethral sphincter. The sphincter is a vertically oriented tubular sheath that surrounds the membranous urethra and prostate. The prostate is enclosed by a capsule composed of collagen, elastin and large amounts of smooth muscle. The prostate is covered by 3 distinct layers of fascia on the anterior, lateral, and posterior aspects. The anterior and anterolateral fascia is in direct continuity of the true capsule; this is the location of the deep dorsal vein of the penis and its tributaries. Laterally, the fascia fuses with the levator fascia.

The outer longitudinal fibers of the detrusor muscle fuse and blend with the fibromuscular tissue of the capsule. The posterior aspect is covered by the rectovesical (Denonvilliers) fascia. The rectovesical fascia is a connective tissue that is located between the anterior wall of the rectum and posterior aspect of the prostate. This fascial layer covers the prostate and seminal vesicles posteriorly and extends caudally to terminate as a fibrous plate just below the urethra at the level of the external urethral sphincter. This is described as a median fibrous raphe which has a distal extension to the level of the central tendon of the perineum. The gland is supported anteriorly by the puboprostatic ligaments and inferiorly by the external urethral sphincter and perineal membrane. The puboprostatic ligaments are actually pubovesical ligaments; however, with the growth of the prostate from puberty, these ligaments have the appearance of terminating into the prostate. The prostate is surrounded by the puborectal portion of the levator ani. The seminal vesicles lie superior to the prostate under the base of the bladder and are approximately 6 cm in length. Each seminal vesicle joins its corresponding ductus deferens to form the ejaculatory duct before entering the prostate [20] [25].

1.1.2 Microscopic Anatomy

The prostate is divide into three zones: transition zone, central zone, and peripheral zone [6][33]. The transition zone accounts for 10% of the prostatic glandular tissue and 20% of the adenocarcinomas. The prostate consists of approximately 70% glandular tissue and 30% fibromuscular stroma [20].

Transition Zone

The prostatic urethra courses the length of the prostate from the level of the bladder neck to the level of the membranous urethra. The epithelium consists of transitional cells similar to bladder epithelium. This transitional zone is where benign prostatic hyperplasia occurs and can lead to bladder outlet obstruction when an adenoma grows to a significant size. When the adenoma grows large enough, it can compress the fibromuscular band surrounding this zone, creating a surgical capsule. The transitional zone is often described as having two lateral lobes and a median lobe that lead to the symptoms of the lower urinary tract symptoms. A urethral crest runs along the posterior midline and disappears at the membranous urethra. On both sides of the urethral crest, there is a grove where the prostatic sinuses exist and drain all of the glandular elements. The urethral crest widens and protrudes from the posterior wall as the seminal colliculus (verumontanum). A small midline pit, the prostatic utricle, is found at the apex of the seminal colliculus. On either side of the utricular orifice, the small slit-like openings to the ejaculatory duct can be found.

Central Zone

The central zone is the area surrounding the ejaculatory ducts. This zone consists of 25% of the glandular tissue. Very few adenocarcinomas are found in this region and can represent as little as 1-5% of these tumours in the prostate.

Peripheral Zone

The peripheral zone of the prostate constitutes 70% of the glandular tissue. This zone covers the posterior and lateral aspects of the prostate. The peripheral zone is the area that is palpated on digital rectal examination (DRE) and represents the area where 70% of adenocarcinomas are found. This area is also the location most commonly affected by chronic prostatitis.

1.1.3 Vascular Supply

Arterial Supply

The arterial supply to the prostate is primarily from the inferior vesicular artery, which originates from the anterior division of the internal iliac (hypogastric) artery [20]. The inferior vesicular artery then branches into two main arterial branches to feed the prostate. The prostatic vessels and the autonomic innervations run between the layers of the lateral prostatic fascia and the prostate. The inferior vesicular artery supplies the base of the bladder, the distal ureters, and the prostate. The first arterial branch is the urethral artery that enters the prostatovesical junction posterolaterally and travels inward perpendicular to the urethra toward the bladder neck at approximately the five o'clock and seven o'clock meridian. The urethral artery then turns caudally and parallel to the urethra to supply the transition zone. This artery is the main arterial supply for the adenomas in benign prostatic hyperplasia. The capsular artery is the second main branch of the prostate. It runs posterolateral to the prostate with the cavernous nerves. This artery enters the prostate at right angles to

supply the glandular tissue. The arterial blood supply to the seminal vessels and ductus deferens comes from the deferential artery or artery of the ductus, a branch from the superior vesicular artery.

Venous Supply

The venous drainage of the prostate starts with the deep dorsal vein, which leaves the penis under the deep penile (Buck) fascia between the corpora cavernosa and then under the pubic arch [20]. This vein then passes anterosuperior to the perineal membrane and divides into 3 major branches: the superficial branch and the right and left branches. The superficial branch travels between the puboprostatic ligaments and lies on top of the prostate and bladder neck. It is outside the anterior prostatic fascia in the retropubic fat and pierces the fascia to drain into the dorsal venous complex. The common trunk of the dorsal venous complex and the lateral venous plexuses are covered by the anterior prostatic fascia and the endopelvic fascia. The lateral plexuses travel postero-laterally and communicate with the pudendal, obturator, and vesical plexus. These veins then communicate with the internal iliac vein.

1.1.4 Neural and Lymphatic Anatomy

Innervations

The autonomic innervations of the prostate arise from the pelvic plexuses formed by the parasympathetic, visceral, efferent, and pre-ganglionic fibers that arise from the sacral levels (S2-S4) and the sympathetic fibers from the thoracolumbar levels (L1-L2) [20]. The pelvic plexus is located beside the rectum approximately seven cm from the anal

verge, with its midpoint located at the level of the tips of the seminal vesicles. The sympathetic and parasympathetic fibers that come from the pelvic plexuses travel to the prostate via the cavernous nerves. The cavernous nerves run postero-lateral to the prostate in the lateral prostatic fascia. The parasympathetic nerves end at the acini and lead to prostatic secretion. The sympathetic nerves lead to contraction of the smooth muscle of the capsule and the stroma. The pudendal nerve is the major nerve supply leading to somatic innervations of the striated sphincter and the levator ani. The preprostatic sphincter and the vesicle neck or internal sphincter is under alpha-adrenergic control.

Lymphatic drainage

The lymphatic drainage of the prostate primarily drains to the obturator and the internal iliac lymphatic channels. There is also lymphatic communication with the external iliac, presacral, and the para-aortic lymph nodes [20].

1.1.5 Role in continence

The mechanisms controlling urinary continence require several coordinated events [35] [38]. The first mechanism is an intact bladder neck with functional internal sphincter. Proximal to the bulbar urethra and distal to the seminal colliculus, the urethral wall, the second mechanism, is composed of smooth muscle and elastic tissue along with the external urethral sphincter. The third component of continence is achieved by the levator ani. The major contributing muscles are the puborectalis complex. This complex forms the urogenital hiatus that flanks the sphincter urethra. The active continence is controlled by the

voluntary contraction of the levator ani musculature which surrounds the apex of the prostate and membranous urethra and the external urethral sphincter. The external urethral sphincter is a cylindrical structure that extends from the external surface of the prostate to the perineal membrane and consists of predominantly slow-twitch striated muscle. The internal sphincter is an extension of the circular smooth muscle of the vesicle neck that ends at the seminal colliculus.

1.2 Prostate cancer

Prostate cancer is one of the most common types of cancer in men [19]. Prostate cancer usually grows slowly and initially remains confined to the prostate gland, where it may not cause serious harm. While some types of prostate cancer grow slowly and may need minimal or no treatment, other types are aggressive and can spread quickly. Prostate cancer that is detected early, when it's still confined to the prostate gland, has a better chance of successful treatment [20].

1.2.1 Symptoms

Prostate cancer may not cause signs or symptoms in its early stages, but if it's more advanced may cause signs and symptoms such as decreased force in the stream of urine, blood in the urine or in the semen, general pain in the lower back, hips or thighs, discomfort in the pelvic area, bone pain and erectile dysfunction [38].

1.2.2 Causes

It's not clear what causes prostate cancer [38]. Doctors know that prostate cancer begins when some cells in your prostate become abnormal. Mutations in the abnormal cells' DNA cause the cells to grow and divide more rapidly than normal cells do. The abnormal cells keep living, when other cells would die. The accumulating abnormal cells form a tumour that can grow to invade nearby tissue. Some abnormal cells can break off and spread (metastasise) to other parts of the body.

1.2.3 Risk factors

Factors that can increase the risk to become ill of prostate cancer are principal four [6] [26]:

- Older age: the risk of prostate cancer increases with age. Prostate cancer is most common in men older than 65.
- Black men have a greater risk of prostate cancer than men of other races. In black men, prostate cancer is also more likely to be aggressive or advanced. It's not clear why this happens.
- Family history of prostate or breast cancer: if a man in his family has had prostate cancer, risk may be increased. Also, a BRCA1 or BRCA2 gene mutation or a very strong history of women with breast cancer, the risk for prostate cancer may be higher.
- Obesity: Obese men diagnosed with prostate cancer may be more likely to have advanced disease that's more difficult to treat.

1.2.4 Complications

Complications [6] [26] of prostate cancer and its treatments principally include:

- Secondary lesions: prostate cancer can spread to nearby organs, such as bladder, or travel through the bloodstream or lymphatic system to the bones or other organs. Prostate cancer that spreads to the bones can cause pain and broken bones. Once prostate cancer has spread to other areas of the body, it may still respond to treatment and may be controlled, but it can no longer be cured.

- Incontinence: both prostate cancer and its treatment can cause urinary incontinence. Treatment for incontinence depends on its severity and the likelihood it will improve over time. Treatment options may include medications, catheters and surgery.
- Erectile dysfunction: erectile dysfunction, as incontinence, can be a result of prostate cancer or its treatment, including surgery, radiation or hormone treatments. Medications, vacuum devices that assist in achieving erection and surgery are available to treat erectile dysfunction.

1.2.5 Tests and diagnosis

Screening tests

Prostate screening tests are the digital rectal exam (DRE) and the prostate-specific antigen (PSA) test [6] [31]. During the DRE, the doctor inserts a gloved, lubricated finger into the rectum to examine the prostate, which is adjacent to the rectum. If the doctor finds any abnormalities in the texture, shape or size of the gland, the patient may need more tests. The second test type provides that blood sample is drawn from a vein in the arm and analyzed for PSA, a substance that's naturally produced by the prostate gland. It's normal for a small amount of PSA to be in the bloodstream; however, if a higher than normal level is found, it may be an indication of prostate infection, inflammation, enlargement or cancer. PSA testing combined with DRE helps identifying prostate cancers at their earliest stages, but studies haven't proved that these tests save lives. For that reason, there is debate about prostate cancer screening.

Diagnosing prostate cancer

If an abnormality is detected on a DRE or PSA test, doctor may recommend tests to determine whether the patient has prostate cancer, such as ultrasound or collecting a sample of prostate tissue [6]. The first technique consists in a small probe, about the size and shape of a cigar, that is inserted into the rectum of the patient, to make a picture of the prostate gland. The second method is a prostate biopsy and it's recommend if the initial test results suggest prostate cancer. Prostate biopsy is often done using a thin needle that's inserted into the prostate to collect tissue. The tissue sample is analyzed in a lab to determine whether cancer cells are present.

Determining whether prostate cancer is aggressive

When a biopsy confirms the presence of cancer, the next step, called grading, is to determine how aggressive the cancer is. The tissue samples are studied, and the cancer cells are compared with healthy prostate cells. The more the cancer cells differ from the healthy cells, the more aggressive the cancer and the more likely it is to spread quickly. More-aggressive cancer cells have a higher grade. The most common scale used to evaluate the grade of prostate cancer cells is called a Gleason score. Scoring combines two numbers and can range from 2 (non aggressive cancer) to 10 (very aggressive cancer) [20] [6].

Determining how far the cancer has spread

Once a prostate cancer diagnosis has been made, the doctor works to determine the extent (stage) of the cancer. If he suspects the cancer may have spread beyond the prostate, can be recommended imag-

ing tests. This methods of inspection are typically: bone scan, ultrasound, computerized tomography scan (CT), magnetic resonance imaging (MRI) and positron emission tomography (PET). The prostate cancer stages [31] [20] are:

- Stage I: it is a very early cancer confined to a small area of the prostate. When viewed under a microscope, the cancer cells aren't considered aggressive.
- Stage II: the cancer size at this stage may still be small but may be considered aggressive when cancer cells are viewed under the microscope. Or cancer may be larger and may have grown invading both sides of the prostate gland.
- Stage III: the cancer has spread beyond the prostate to the seminal vesicles or other nearby tissues.
- Stage IV: the cancer has grown to invade nearby organs, such as the bladder, or spread to lymph nodes, bones, lungs or other organs.

1.3 Radiotherapy

Radiation therapy is the medical uses ionizing radiation, generally as part of cancer treatment to control or kill malignant cells. Radiation therapy may be curative in a number of cancer types if they are localized to one area of the body. It may also be used as part of adjutant therapy, to prevent tumour recurrence after surgery to remove a primary malignant tumour. Radiation therapy is synergistic with chemotherapy, and has been used before, during, and after chemotherapy in susceptible cancers [12] [29].

Radiation therapy is commonly applied because of its ability to control cell growth. Ionizing radiation works by damaging the DNA of exposed tissue leading to cellular death. To spare normal tissues, shaped radiation beams are aimed from several angles of exposure to intersect at the tumour, providing a much larger absorbed dose there than in the surrounding, healthy tissue. Besides the tumour itself, the radiation fields may also include the draining lymph nodes if they are clinically or radiologically involved with tumour, or if there is thought to be a risk of sub-clinical malignant spread. It is necessary to include a margin of normal tissue around the tumour to allow for uncertainties in daily set-up and internal tumour motion. These uncertainties can be caused by internal movement (for example, respiration and bladder filling) and movement of external skin marks relative to the tumour position [20].

Radiation oncology is the medical speciality concerned with prescribing radiation, and is distinct from radiology, the use of radiation in medical imaging and diagnosis. Radiation may be prescribed by a radiation oncologist with intent to cure or for adjutant therapy. It is

also common to combine radiation therapy with surgery, chemotherapy, hormone therapy, immunotherapy or some mixture of the four [3]. The precise treatment intent (curative, adjutant, neo-adjutant, therapeutic, or palliative) will depend on the tumour type, location, and stage, as well as the general health of the patient. The underlying figure 1.2 shows how radiotherapy is performed.

Figure 1.2: Image of a classical radiotherapy.

1.3.1 Mechanism of action

Radiation therapy works by damaging the DNA of cancerous cells. DNA damage is caused by one of two types of energy: photon or charged particle [3]. This damage can be direct or indirect ionization of the atoms which make up the DNA chain. Direct action occurs when alpha particles, beta particles or x-rays create ions which physically break one or both of the sugar phosphate backbones or break the base pairs of the DNA (adenine, thymine guanine and cytosine) that are held together by weak hydrogen bonds. Indirect ionization happens

as a result of the ionization of water, forming free radicals, notably hydroxyl radicals, which then damage the DNA. In photon therapy, most of the radiation effect is through free radicals [20]. Because cells have mechanisms for repairing single-strand DNA damage, double-stranded DNA breaks prove to be the most significant technique to cause cell death. Cancer cells are generally less differentiated and more similar to stem cell; they reproduce more than most healthy differentiated cells, and have a diminished ability to repair sub-lethal damage. Single-strand DNA damage is then passed on through cell division; damage to the DNA of cancerous cell accumulates, causing them to die or reproduce more slowly. One of the major limitations of photon radiation therapy is that the cells of solid tumours become deficient in oxygen. Solid tumours can outgrow their blood supply, causing a low-oxygen state known as hypoxia. Oxygen is a potent radio-sensitizer, increasing the effectiveness of a given dose of radiation by forming DNA-damaging free radicals. Tumour cells in a hypoxic environment may be as much as 2 to 3 times more resistant to radiation damage than those in a normal oxygen environment.

Charged particles such as proton, boron, carbon, and neon ions can cause direct damage to cancer cell DNA through high-LET (linear energy transfer) and have an anti-tumour effect independent of tumour oxygen supply because these particles act mostly via direct energy transfer usually causing double-stranded DNA breaks. Due to their relatively large mass, protons and other charged particles have little lateral side scatter in the tissue does not broaden much, staying focused on the tumour shape, and delivering small dose side-effects to surrounding tissue.

Proton therapy is a good example of the different effects of intensity-modulated radiation therapy (IMRT) [8] [3] and charged particle therapy. This second procedure reduces damage to healthy tissue between the charged particle radiation source and the tumour and sets a finite range for tissue damage after the tumour has been reached. In contrast, IMRT's use of uncharged particles causes its energy to damage healthy cells when it exits the body. This exiting damage is not therapeutic, can increase treatment side effects, and increases the probability of secondary cancer induction. This difference is very important in cases where the close proximity of other organs makes any stray ionization very damaging (for example, head and neck cancers). This x-ray exposure is especially bad for children, due to their growing bodies, and they have a 30% chance of a second malignancy after 5 years post initial RT.

1.3.2 Dose

The amount of radiation used in photon radiation therapy is measured in gray (Gy), and varies depending on the type and stage of cancer being treated [6]. For curative cases, the typical dose for a solid epithelial tumour ranges from 60 to 80 Gy, while lymphomas are treated with 20 to 40 Gy. Preventative doses are typically around between 45 and 60 Gy in 1.8 - 2 Gy fractions (for breast, head, and neck cancers). Time in which the patient is receiving chemotherapy, patient comorbidities, time radiation therapy is being administered before or after surgery and the degree of success of surgery are factors considered by radiation oncologists when selecting a dose [38]. Delivery parameters of a prescribed dose are determined during treatment planning.

Fractionation

The total dose is fractionated for several important reasons. Fractionation allows normal cells time to recover, while tumour cells are generally less efficient in repair between fractions. Fractionation also allows tumour cells, that were in a relatively radio-resistant phase of the cell cycle during one treatment, to cycle into a sensitive phase of the cycle before the next fraction is given [31] [3].

Schedules for fractionation

One fractionation schedule that is increasingly being used and continues to be studied is hypo fractionation [20] [3]. This is a radiation treatment in which the total dose of radiation is divided into large doses. Typical doses vary significantly by cancer type, from 2.2 Gy/fraction to 20 Gy/fraction. The logic behind hypo fractionation is to lessen the possibility of the cancer returning by not giving the cells enough time to reproduce and also to exploit the unique biological radiation sensitivity of some tumours. One of the best-known fractionation schedules is Continuous Hyper-fractionated Accelerated Radiation therapy (CHART). CHART, used to treat for example prostate or lung cancer, consists of three smaller fractions per day. Another increasingly well-known alternative fractionation schedule, used to treat breast cancer, is called Accelerated Partial Breast Irradiation (APBI). APBI can be performed with either brachytherapy [paragraph 1.3.3] or with external beam radiation [paragraph 1.3.3]. APBI normally involves two high-dose fractions per day for five days, compared to whole breast irradiation, in which a single, smaller fraction is given five times a week over a six-to-seven-week period.

1.3.3 Types

Historically, the three main divisions of radiation therapy are external beam radiation therapy (EBRT or XRT) or teletherapy, brachytherapy or sealed source radiation therapy, and systemic radioisotope therapy or unsealed source radiotherapy. The differences are related to the position of the radiation source; external is outside the body, brachytherapy uses sealed radioactive sources placed precisely in the area under treatment and systemic radioisotopes are given by infusion or oral ingestion.

Brachytherapy [41] can use temporary or permanent placement of radioactive sources. The temporary sources are usually placed by a technique called "afterloading". In afterloading a hollow tube or applicator is placed surgically in the organ to be treated, and the sources are loaded into the applicator after the applicator is implanted. This minimizes radiation exposure to health care personnel.

Particle therapy is a special case of external beam radiation therapy where the particles are protons or heavier ions.

Intraoperative radiation therapy (IORT) is a special type of radiation therapy that is delivered immediately after surgical removal of the cancer [3].

External beam radiotherapy

External beam radiotherapy or teletherapy is the most common form of radiotherapy [11]. The patient sits or lies on a couch and an external source of radiation is pointed at a particular part of the body. Kilovoltage ("superficial") X-rays are used for treating skin cancer and superficial structures. Megavoltage ("deep") X-rays are used to treat

deep-seated tumours (for example bladder, bowel, prostate, lung, or brain). While X-ray and electron beams are by far the most widely used sources for external beam radiotherapy, a small number of centres operate experimental and pilot programs employing heavier particle beams, particularly proton sources.
Conventional external beam radiation therapy (2DXRT) is delivered via two-dimensional beams using linear accelerator machines [3]. 2DXRT mainly consists of a single beam of radiation delivered to the patient from several directions: often front or back, and both sides. Conventional refers to the way the treatment is planned or simulated on a specially calibrated diagnostic x-ray machine known as a simulator because it recreates the linear accelerator actions (or sometimes by eye), and to the usually well-established arrangements of the radiation beams to achieve a desired plan. The aim of simulation is to accurately target or localize the volume which is to be treated. This technique is well established and is generally quick and reliable. The worry is that some high-dose treatments may be limited by the radiation toxicity capacity of healthy tissues which lay close to the target tumour volume. An example of this problem is seen in radiation of the prostate gland, where the sensitivity of the adjacent rectum limited the dose which could be safely prescribed using 2DXRT planning to such an extent that tumour control may not be easily achievable.

A new method to reduce rectal radiation injury in prostate cancer patients involves the use of an absorbable spacer placed between the prostate and rectum. MRI showing hydrogel spacer pushing the rectum away from the prostate during radiotherapy. Prostate Rectum Spacers should be compatible with all prostate cancer radiotherapy

treatments including 3D conformal, IMRT and stereotactic radiation and brachytherapy.

Planning of radiation therapy The planning of radiation therapy treatment has been revolutionized by the ability to delineate tumours and adjacent normal structures in three dimensions using specialized CT and/or MRI scanners and planning software. Virtual simulation, the most basic form of planning, allows more accurate placement of radiation beams than is possible using conventional X-rays, where soft-tissue structures are often difficult to assess and normal tissues difficult to protect. An enhancement of virtual simulation is 3-dimensional conformal radiation therapy (3DCRT), in which the profile of each radiation beam is shaped to fit the profile of the target from a beam's eye view (BEV) using a multi leaf collimator (MLC) and a variable number of beams. When the treatment volume conforms to the shape of the tumour, the relative toxicity of radiation to the surrounding normal tissues is reduced, allowing a higher dose of radiation to be delivered to the tumour than conventional techniques would allow. Intensity-modulated radiation therapy (IMRT) is an advanced type of high-precision radiation that is the next generation of 3DCRT. IMRT also improves the ability to conform the treatment volume to concave tumour shapes, for example when the tumour is wrapped around a vulnerable structure such as the spinal cord or a major organ or blood vessel.

Brachytherapy

Brachytherapy [41] is commonly used as an effective treatment for cervical, prostate, breast and skin cancer and can also be used to treat tumours in many other body sites. In brachytherapy, radiation sources are precisely placed directly at the site of the cancerous tumour. This means that the irradiation only affects a very localized area to radiation of healthy tissues further away from the sources is reduced. These characteristics provide advantages over external beam radiation therapy; in fact the tumour can be treated with very high doses of localized radiation, whilst reducing the probability of unnecessary damage to surrounding healthy tissues. A course of brachytherapy can often be completed in less time than other radiation therapy techniques. This can help to reduce the chance of surviving cancer cells dividing and growing in the intervals between each radiation therapy dose. This approach decreases the exposure of healthy tissue and resulting side effects, compared both to external beam radiation therapy and older methods of breast brachytherapy.

Radioisotope therapy

Systemic radioisotope therapy is a form of targeted therapy [20]. Targeting can be due to the chemical properties of the isotope such as radioiodine which is specifically absorbed by the thyroid gland a thousandfold better than other bodily organs. Targeting can also be achieved by attaching the radioisotope to another molecule or antibody to guide it to the target tissue.

The radioisotopes are delivered through infusion (into the bloodstream) or ingestion. These microspheres are used for the treatment

approach known as selective internal radiation therapy. The microspheres are approximately 30 μm in diameter and are delivered directly into the artery supplying blood to the tumours. These treatments begin by guiding a catheter up through the femoral artery in the leg, navigating to the desired target site and administering treatment. The blood feeding the tumour will carry the microspheres directly to the tumour enabling a more selective approach than traditional systemic chemotherapy.

1.3.4 Side effects

Side effects are caused by damage to healthy cells [8]. Different cells and tissues in the body tolerate radiation differently. The cells most affected are rapidly dividing cells, such as skin cells, cells lining the mouth and gastrointestinal tract or blood cells in the bone marrow. Side effects can occur with any type of treatment, but not everyone has them or experiences them in the same way. General side effects of radiation therapy can occur when radiation is given to any area of the body, but will depend mainly on the specific area or organs being treated, the size of the area being treated, the type of radiation therapy, the amount of radiation given, the treatment schedule, a person's overall health and on other medicines the person is taking. Side effects can happen any time during, immediately after or a few days or weeks after radiation therapy. Most side effects generally go away within two months of finishing treatment. However, some side effects may continue after treatment is over because it takes time for healthy cells to recover from the effects of radiation therapy. Late side effects can occur months or years after treatment. If doses of radiation are high

enough, some cells may not be able to repair themselves. As a result, some side effects may last a long time or be permanent [6]. A short description of the most commons side effects is write in the followings paragraphs.

Fatigue. Fatigue is one of the most common side effects of radiation therapy and it may be caused by anaemia, poor appetite or depression. Fatigue may also be related to toxic substances that are produced when cancer cells break down and die. During radiation therapy, the body uses more energy to heal itself, so fatigue will not always be relieved by rest. Making frequent, daily trips for radiation treatments can also be tiring. Radiation therapy to any area of the body can make a person feel more tired than usual, but fatigue is more common when larger areas of the body are treated. Anaemia is more likely to occur when the treatment area includes where blood cells are formed in the bone marrow, such as the pelvic bones. Fatigue usually occurs during or after the second week of radiation therapy. Symptoms of fatigue may increase or become more severe over the course of treatment. Fatigue in majors part of cases goes away gradually after treatment has ended, but some people continue to feel tired for several weeks or months after radiation therapy.

Skin reactions. Skin reactions occur because external beam radiation travels through the skin to reach the area being targeted for treatment. The skin in the radiated area may become red, dry or itchy. It may change colour becoming darker or tanned looking. Most skin reactions occur within the first 2 weeks of receiving radiation therapy. They usually go away a few weeks after treatment, but some skin

changes, like skin darkening or scarring, can be permanent. Some people do not experience any skin reactions with radiation therapy.

Changes in appetite. Radiation therapy can affect a person's appetite in a number of ways. Radiation therapy to the head and neck area can cause temporary changes in taste or smell, which can make foods seem less appetizing. Some people lose interest in food completely and don't eat, even though they know they need to. Loss of appetite is a common problem and can lead to weight loss. Some people may gain weight from frequent snacking to control nausea during treatment. Loss of appetite typically occurs after side effects like mouth sores, dry mouth, difficulty swallowing and nausea or vomiting develop. It may continue for 2 or 3 weeks or longer after treatment has ended. Maintaining good nutrition during and after radiation therapy is important to help a person recover from treatment.

Hair loss. Hair loss (alopecia) only occurs in the area being treated with radiation therapy. Thinning or loss of hair can occur in any area where radiation is directed. The extent of hair loss and regrowth varies from person to person and depends on the dose of radiation. Hair loss can begin about 2 or 3 weeks after radiation therapy starts. Smaller doses of radiation usually result in temporary hair loss. Permanent hair loss is more common at higher doses. When hair regrows, usually about 3-6 months after radiation therapy is finished, the colour or texture may be different and it may grow back thinner or patchy.

Radiation sickness. Radiation sickness is characterized by loss of appetite, nausea and vomiting. This is a common side effect if the

stomach and abdomen are in the treatment area. It can also occur as a general side effect regardless of the area being treated. Radiation sickness is due to toxic substances that are released when tumour cells break down and die. Radiation sickness usually goes away a few weeks after external beam radiation therapy is finished.

Bone marrow suppression. Bone marrow suppression is a condition in which one or more of the main types of blood cells are decreased. A low white blood cell count (neutropenia or leukopenia) increases the risk of infection, a low platelet count (thrombocytopenia) increases the risk of bruising and bleeding while a low red blood cell count (anemia) causes fatigue, paleness and malaise.

Reduced bone growth. Reduced bone growth occurs because of radiation's effect on the rapidly dividing immature cells of bones that lie in the treatment area. This is most noticeable in very young children because most of their bones have not matured to the point where they can withstand radiation. The child's height or limb length can be shortened. Scoliosis (curved spine), kyphosis (hunchback) or spinal shortening can also occur. In addition, bones treated with radiation tend to break easily.

Anxiety or depression. Each person reacts differently to a cancer diagnosis and will cope in different ways. Starting radiation therapy can lead to new worries and fears and may cause anxiety, sadness and depression.

Sleep problems. Sleep problems, especially insomnia, are common during treatment. Signs of insomnia include: being unable to fall asleep, waking up often during the night and waking up very early and being unable to go back to sleep feeling sleepy during the daytime

Changes in sexuality. Some people may experience changes in their feelings about and attitudes toward sexuality as they go through radiation therapy. Some people are less interested in sex because of the physical and emotional stresses of having cancer and getting radiation therapy.

Second cancers. A very small number of people develop a second cancer caused by radiation therapy. The benefit of treating a person's cancer usually far outweighs the risk of developing a second cancer from radiation therapy. People who receive both chemotherapy and radiation therapy have the highest risk of developing a second cancer. A second cancer can develop a few years after radiation treatment, but most do not occur for 10-20 years or more after treatment.

1.4 A diagnostic instrument: Magnetic Resonance Imaging

The Magnetic Resonance Imaging (MRI) [13] is an important diagnostic tool that allows to obtain three-dimensional images and is particularly suitable examination of the soft tissues, with rich water content: muscles, internal organs, blood vessels, ligaments. It fails to provide good information in different fields from the trauma to the cancer. In particular, abdominal magnetic resonance imaging is a test that provides detailed images of the entire area below the diaphragm and is often used to clarify the results of previous ultrasound examination or computed tomography. The discovery of MRI is due to Felix Bloch and Edward Purcell (1946, Nobel in 1952) [27]. It is consisted in the resonance of H^1 nuclei (protons) and of other nuclei characterized by an odd number of protons and/or neutrons when exposed to an RF pulse proportional to the external magnetic field intensity. Differently from other investigating techniques, ionizing radiations are not required: only magnetic field and RF pulses are used, which can go through tissues without inducing damages. In the field of urology and andrology, MRI has been for years the best choice in the classification and evaluation of prostate cancers; it allows an accurate assessment of the extension and the local and regional dimension of the tumour, provides morphological parameters for the planning of subsequent treatments or surgical therapy for the indication of a "neo-adjuvant".
Magnetic resonance imaging is a "multi planar" and "multi parametric" imaging technique: multi planar because it can acquire imaging planes axial, coronal or sagittal; multi parametric because of the use

of reference parameters such as the proton density and the relaxation times T1 and T2 [22]. The information obtained from MRI are different in nature from those of other imaging methods, because it is possible the discrimination between tissues based on their biochemical composition. Regarding the CT, it is indicated when there is no need to have a very high spatial resolution ($\approx 1mm$), but against a slower temporal resolution. Furthermore, it is more useful in the event of localized lesions in tissue close to bone structures, which may not be detectable by X-rays.

1.4.1 Operating Principle

MRI operating principle is based on the fact that each atomic nucleus is associated with a mechanical quantity that describes the properties of the nucleus itself: the *spin number I*. I can take on only certain values (as 0, $\frac{1}{2}$, $\frac{3}{2}$, 1... until 6); nuclei that have a odd number of protons and/or neutrons have an non-zero number of spin. These nuclei, in addition, possess an angular momentum vector $\vec{J}$ called *spin*, which can be represented by a rotation of the spheric nucleus around an axis inside. Each nucleus can thus be seen as a magnetic dipole and the intensity of this vector can be measured by the follower equation:

$$J = \frac{h}{2\pi}\sqrt{I(I+1)} \tag{1.1}$$

where h = Plank's constant = 6.626 $10^{-34} Js$.

A change of rotation of the nucleus always produces a magnetic moment $\vec{\mu}$, which is associated to angular momentum vector $\vec{J}$, according to relation:

$$\vec{\mu}=\gamma\vec{J} \tag{1.2}$$

where γ is the proportionality coefficient known as *gyromagnetic ratio* of the nucleus. Combining the 1.1 and the 1.2:

$$\vec{\mu} = \gamma\frac{h}{2\pi}\sqrt{I(I+1)} \tag{1.3}$$

From this relation it can deduce that nuclei with spin I=0 have $\mu = 0$, thus can not be observed with MR.

In the normal condition, the orientation of magnetic moments of each nuclei has a random distribution and it is said that nuclei are degenerate, having the same energy. In this case (Figure 1.3), in the absence of an external magnetic field, the dipoles are free to orient randomly and their *global magnetization* $\vec{M}=\Sigma\ \vec{\mu_i}$ is zero.
Instead, when a nucleus with spin I is placed in a static external magnetic field B_0 (generally directed along z-axis), the magnetic moment μ can assume 2I+1 possible orientations corresponding to different energy levels.

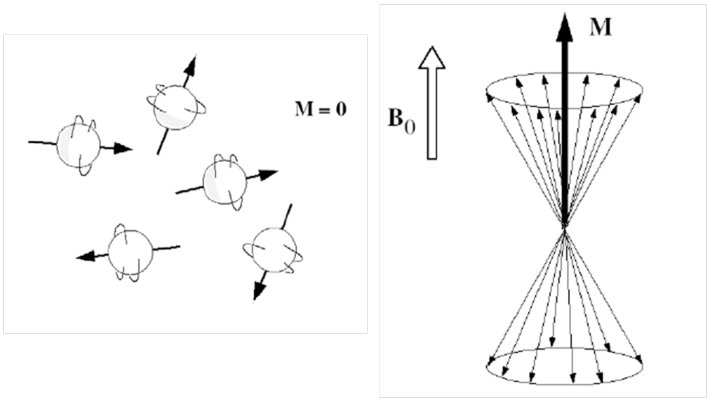

Figure 1.3: In the absence of external magnetic field, the dipoles are oriented random and therefore the global magnetization $\vec{M} = 0$. Instead, from the action of the static magnetic field B_0 , the nuclei contained in the tissues change orientation, aligning to B_0.

The energy that corresponds to these levels is expressed by the equation:

$$\text{E}=-\mu B_0=-\mu_z B_0=-\gamma\frac{h}{2\pi}m_I B_0 \tag{1.4}$$

where m_I is defined as *quantum number directional* and can take values ranging +I (+I-1) ... -I.
In particular hydrogen H^1, thanks to its abundance in biological tissue and the physical properties which facilitate the detection of the MR signal, is the nucleus normally used for MR imaging for diagnostic purposes.
Conventionality, in MRI are considered nuclei with I=$\frac{1}{2}$ and m_I=$\pm\frac{1}{2}$, therefore characterized by two energy levels:

- spin-up, parallel to B_0, at minimum energy: E↑=-$\frac{1}{2}\gamma\frac{h}{2\pi}B_0$;
- spin-down, anti-parallel to B_0, at maximum energy: E↓=+$\frac{1}{2}\gamma\frac{h}{2\pi}B_0$.

The energetic gap ΔE between spin-up and spin-down results
ΔE= E↓ - E↑= $\gamma \frac{h}{2\pi} B_0$
If positioned inside a magnetic field, the magnetic dipole has a precession movement around the field axis. The frequency, to which the dipoles move, is proportional to the intensity of the magnetic field B_0 and is called *Larmor frequency*. It is defined by equation:

$$f_{Larmor} = h\frac{B_0}{2\pi} = \gamma B_0 \tag{1.5}$$

From this relation, it is obtained that increasing the intensity of the magnetic field B_0, the frequency f increases, that is the speed of rotation of the nucleus around B_0 increases. Nuclei are distributed between the energetic levels according to the Boltzmann's equation:

$$\frac{N_\beta}{N_\alpha} = e^{-\frac{\Delta E}{K_\beta T}} \tag{1.6}$$

where N_α and N_β are nuclei respectively in the ground state and excited state, K_β the Boltzmann's constant= 1.3805 $10^{-23} JK^{-1}$ and T is the absolute temperature in Kelvin.
This energy difference is not actually very high compared to the average energy of the system in balance, consequently the population of the various energy levels are nearly equal.

When each dipole is placed in a magnetic field, it is necessary to apply an *external torque moment* $\vec{\tau}_{ext}$ to contrast the torque moment exercised from magnetic field, in order to maintain balance the dipole; $\vec{\tau}_{ext}$ is zero if $\vec{B_0}$ and dipole are aligned. The torque moment exercised on the dipole from magnetic field $\vec{B_0}$ is:

$$\vec{\tau} = \vec{\mu} \times \vec{B_0} = \gamma \vec{J} \times \vec{B_0} \tag{1.7}$$

Remembering that $\vec{\tau} = \frac{d\vec{J}}{dt}$, the equation of motion for isolated spins is:

$$\frac{d\vec{\mu}}{dt} = \gamma \, \vec{\mu} \times \vec{B_0} \tag{1.8}$$

This solutions describe a particular phenomenon called *nuclear precession.*

The magnetization

In the reality, a single nucleus or a single magnetic moment μ is never seen but the combined effect of all nuclei are registered. When the system is placed inside the external magnetic field $\vec{B_0}$, appears a macroscopic magnetization $\vec{M_0}$ (as longitudinal magnetization) oriented as $\vec{B_0}$ and with modulus proportional to the number of excited magnetic dipoles, that process with their Larmor frequency.

During a MR exam, the patient or a part of his body are introduced in a large cylinder machine, which allows both to generate the magnetic field and to reveal the waves emitted in response from the affected tissues. From the action of the static magnetic field $\vec{B_0}$[1], the nuclei (hydrogen atoms contained in the tissues) change orientation, aligning and then return to the random state at the end of this effect. This macroscopic magnetization along the direction $\vec{B_0}$ can not be measured and therefore, in order to measure this effect, it is necessary to transfer it in a plane orthogonal to B_0. For this purpose, a rotating external magnetic field $\vec{B_1}$ generated by radio-frequency (RF) coils is added to $\vec{B_0}$, so that it is possible to rotate the magnetization of the protons of an arbitrary angle called flip angle $\alpha = \Omega_{B1}\delta t = \gamma B_1 \delta t$, with angular velocity Ω_{B1} and duration δt (Figure 1.4).

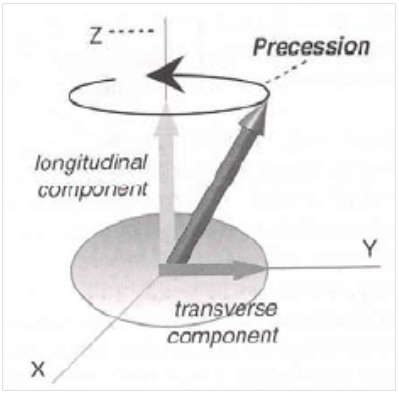

Figure 1.4: Radio-frequency excitation by RF pulse=f$_{Larmor}$. It is got a magnetization rotated by an arbitrary angle, as flip angle

.

Changing the RF pulse amplitude B_1 and/or duration δt, a vector M that may take any orientation can be created.

[1]The intensity of the magnetic field B_0 can vary from 1 to 3 Tesla for the machines currently selling for diagnostic purposes

Nuclei with Larmor angular velocity = Ω_{B1} achieve a condition of resonance and emit a signal, which is detected by the tool and processed by a computer to obtain images of the body's areas of interest. Turning off the radio frequency pulse (B_1 off), the spins of the protons will tend to gradually get back to their initial alignment along the field B_0=B_z (relaxation phenomenon). The longitudinal component M_z of the macroscopic magnetization try to take the initial value of balance M_0 (longitudinal relaxation); instead, the transverse component M_{xy} decays to zero (transversal relaxation) according to the relations:

$$\begin{cases} M_z = M_z^0(1 - e^{\frac{-t}{T1}}) \\ M_{xy} = M_{xy}^0 e^{\frac{-t}{T2}} \end{cases}$$

where M_z^0 is the longitudinal magnetization at final equilibrium and M_{xy} is magnetization on transverse plane immediately after RF pulse.

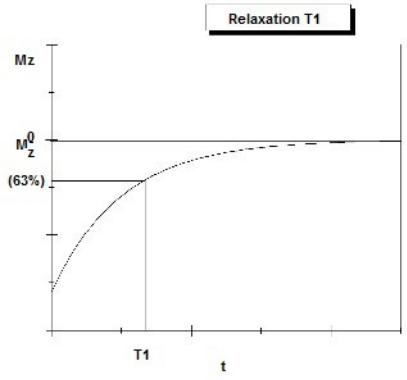

Figure 1.5: The longitudinal component M_z

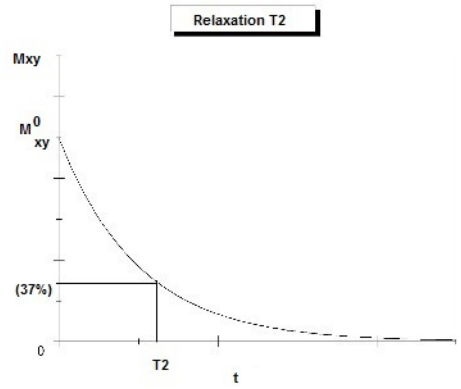

Figure 1.6: The transverse component M_{xy}

In order to describe the variation in time of the main magnetization respect to the variables M, B and γ, the **Bloch's equations** is used, that is:

$$\frac{d\vec{M}}{dt}=\gamma\ (\vec{M}\times\vec{B})\ \text{-}\ \vec{R}(\vec{M}-M_0) \tag{1.9}$$

where $\mathbf{B}=B_0+B_1$ and $\mathbf{R}$=relaxation matrix

$$R=\begin{bmatrix}\frac{1}{T2} & 0 & 0\\ 0 & \frac{1}{T2} & 0\\ 0 & 0 & \frac{1}{T1}\end{bmatrix}$$

Decomposing the equation 1.9 in the three directions, it is obtained:

$$\begin{cases}\frac{dM_z}{dt}=\gamma(M_xB_y)-(M_yB_x)-\frac{1}{T_1}(M_z-M_0)\\ \frac{dM_x}{dt}=\gamma(M_yB_z)-(M_zB_y)-\frac{M_z}{T_2}\\ \frac{dM_y}{dt}=\gamma(M_zB_x)-(M_xB_z)-\frac{M_y}{T_2}\end{cases}$$

FID

Sending the radio-frequency pulse on the atoms included in the magnetic field are determined mainly two things:

1. the synchronization of the protons in the same phase of precession (rotate not only at the same frequency but also in a coordinated manner); when protons precede in phase with each other, it generates a transverse magnetization vector $\vec{M}$, which rotates in the xy plane. This vector, in turn, generates a small detectable current in the receiving circuit (antenna).

An RF pulse capable of shifting the magnetization M in the xy plane is defined pulse of 90°;

2. the shift of some protons from the lower energy level (parallel to $\vec{B_0}$) to the higher energy level (anti-parallel to $\vec{B_0}$). An RF pulse of duration or intensity double compared to that of 90° is able to reverse the magnetization vector $\vec{M}$ in anti parallel position with respect to B_0 and is therefore said pulse of 180°.

Once ceased the RF pulse occurs:

1. the gradual de-synchronization of the precession of the protons, resulting in the decay of the transverse magnetization;

2. a return to a lower energy level by the protons that had been reversed by 180°.

After the application of RF pulse, the magnetization vector $\vec{M}$ generates itself a magnetic field oscillating at RF; this can be revealed because it is capable of inducing an alternating current in a coil, in the same coil that is used to generate the $\vec{B_1}$ field. The signal induced by the magnetization vector increases during the application of RF pulse and after deactivation of the B_1, this pulse decays to zero due to the phenomenon of relaxation. This decayed signal, obtained although the absence of $\vec{B_1}$ field, is called *Free Induction Decay* (FID). The decay time of this signal is exponential, with two distinct time constants: the first is known as T1 and the second as T2.

Interaction parameters of the tissue

The contrast in the MRI depends on several magnetic properties of tissues. Although there are many parameters that affects the signal from the observed sample, the most important three are: the proton density, T1 and T2. This parameters normally assume values different for several tissues and also for different areas of the same tissue, that can be in a state physiological or pathological.

- **proton density** ρ: is the number of the protons (hydrogen atoms belong to the water molecules, that displace during an MRI exam) for unit volume, proportional to density of water in the tissues. For example, the bone has a density of water very low; the blood, instead, very high. The intensity of the signal immediately after the end of the excitation pulse 90 is proportional to the proton density: the higher the proton density, the grater the amplitude of the signal.

- **spin-lattice relaxation**: is characterized by the time constant T1 [2]. It indicates the rapidity with which the longitudinal magnetization reconstructs, directed along the direction of the main field $\vec{B_0}$ and depends on the interaction between protons and surrounding molecules. The biological tissue can have T2 varying between 50 and 150 ms. Unlike the T1, the T2 is little influenced by the power of B_0.

[2] T1 can be also expressed as the time required since 63% of the nuclei regains its balanced state, after an RF pulse has altered their position of 90°.

- **spin-spin relaxation**: is characterized by the time constant T2 [3]. It indicates the rapidity with which it destroys the component of transverse magnetization in ideal conditions, and depends on the mutual interaction of neighbours protons. The biological tissues, immersed in a magnetic field intensity of 0.1-0.5 T, can have T1 varying between 300 and 700 ms.

Once the magnetization vector M is back to its equilibrium value M_0, parallel to B_0, there is no possibility of having a non-zero transverse magnetization. For this reason T2 is always less or equal to T1. When the net magnetization in the xy plane goes to zero, the longitudinal magnetization grows in until it is had M_0 along z. In the reality, the combination of two factors contribute to the decay of transverse magnetization:

1. molecular interactions (said to lead to a pure T2 molecular effect);
2. variations in B_0 (said to lead to an inhomogeneous T2 effect).

The combined time constant is called T2*. The relationship between the T2 from molecular processes and that from inhomogeneities in the magnetic field is the following:

$$\frac{1}{T2*} = \frac{1}{T2} + \frac{1}{T2_{inhomo}} \tag{1.10}$$

[3] T2 is the time required since the phase shift of the nuclei leads to the reduction of the transverse component M_{xy} of 63%.

Spatial Coding

In 1973 Paul Lauterbur and then Peter Mansfield understood that the magnetic resonance phenomenon could be employed for medical image generation through also the use of magnetic field gradients.
They discovered that the use of gradients in the magnetic field gave signals that rapidly and effectively could be analysed and transformed to an image. This was an essential step in order to obtain MR images. Mansfield also showed how extremely rapid imaging could be achieved by very fast gradient variations (so called echo-planar scanning).
The contribute to FID signal of different voxels must be discriminated to create images.
In order to create a static magnetic field of spatially variant intensity, three magnetic field gradients (G_x, G_y, G_z) are properly added to B_0. The intensity of gradients G_x, G_y, G_z is small if compared to the intensity of B_0.
These gradients will allow to select the slice and encoding in phase and frequency the individual voxels, determining their location in the image plane.
They impose linear changes in all 3 dimensions of the magnetic field within the patient: as a result of these changes, the precession frequency of the protons is linearly dependent from their position in space.

slice selection A magnetic field gradient G_z is applied in the same instant of RF pulse along an axis z perpendicular to the image plane to select a slice, since all protons are excited only in z = z_p, at the same Larmor frequency defined as:

$$f_{Larmor}=\gamma(B_0+G_z z_p) \tag{1.11}$$

Once the slice is selected, the FID signal measured results to be proportional to two separate components:

$$\text{FID}=\iint \text{I(x,y)}\ e^{j(yG_y t_y)}\ e^{j(xG_x t_x)}\ dx\ dy \tag{1.12}$$

where the phase encoding and the frequency encoding are respectively G_x and G_y and I (x, y) is the useful information, which depends on the proton density, T1 and T2.

phase encoding Turning off G_z, a magnetic field gradient along a y-axis G_x is applied for the phase encoding to locate one of the two dimensions of the image plane xy. The phase encoding is applied with G_x maintaining for a time t_x after RF stimulation but before the acquisition of the FID. Since a single phase encoding is not sufficient to obtain spatial information, it is necessary that the sequence is repeated a number of times to obtain a significant sample along the direction of the phase. This operation is replicated N_x times, where N_x is the number of lines in the image to obtain. The frequency encoding may be used to localize the spins in the second spatial direction.

frequency encoding Once off G_x, a magnetic field gradient G_y along a x-axis is applied for the frequency encoding to locate the second dimension of the image plane xy. The frequency encoding is obtained

during the acquisition of the FID. As a results, a linear variation along the space of the emission frequency of the protons will be had. The acquired signal is the sum of signals at different frequencies, which can be obtained through the Fourier Transform. As for phase encoding, also for frequency encoding a single frequency is not sufficient to obtain spatial information: it is necessary to repeat the sequence a number of times sufficient to obtain a significant sample along the direction of the frequency. The measures of the FID are digitized in N_y samples, where N_y represents the number of columns of the image to be obtained, sampled at time instants t_y. The application of a gradient along a direction ensures that the Larmor frequency of the atoms varies linearly along that direction. As a result, the body inside the magnet is divided into isofrequential parallel planes. A radio-frequency pulse at a specific frequency (monochrome) applied while the gradient is active, will excite a single plane, leaving in balanced condition all the others. This means that in the absence of a magnetic gradient FID which process at the same Larmor frequency, regardless of the selected slice, are obtained. The whole procedure of spatial coding is summarized in Figure 1.7. The series of signals thus acquired, is appropriately digitized and stored in a matrix called *k-space*.

K-space

The evolution of a spin system after excitation is studied more easily in the K-space [4]. The K-space is important for the formation of MR images because it is in the matrix of the K-space stores the acquired MR signals. This space is the domain of the Fourier Transform of

[4] K stands for the wave number K = $\frac{2\pi}{\lambda}$, with components K_x,K_y and K_z

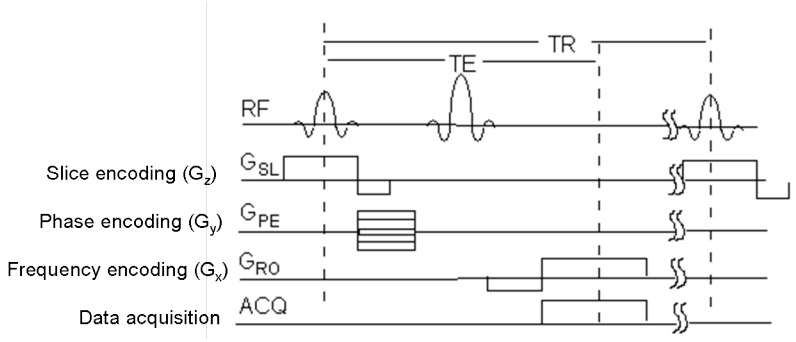

Figure 1.7: The simplest FT imaging sequence contains a 90° slice selective pulse, a slice selection gradient pulse, a phase encoding gradient pulse, a frequency encoding gradient pulse, and a acquired signal.

the MR image that it should be achieved. The images can be decomposed into the sum of sine and cosine waves with different frequency and orientation. The K-space is the set of coefficients that constitute the weight factor of these sine and cosine waves. The coordinates of the K-space are called *spatial frequencies* and their units of measure are *cycles per unit length*. Thus, the spatial frequencies K_x and K_y correspond to a 2D image coordinates x and y. The K-space contains information on the intensity of the various edges of the image rather than the spatial distributions of the various anatomical structures, and these spatial distributions are represented in MR images. The images are transformed from the spatial domain to the K-space using an Inverse Fourier Transform, as will be described later. Each point of the K-space contains information on the entire image MR. The centre of K-space contains information on the coarse structure of the image, while the regions more distant from the centre encode the details. Therefore, the high spatial frequencies (high values K_x and K_y) give information on the details of the elements of the image, while low frequencies coarser spatial provide information on the structure of

the image. The transition from coarse to detail information is gradual from the centre of K-space to its extremes. Sometimes, to get the MRI can be useful not acquire all the K-space but only a part of it, especially if it is want to reduce the data acquisition time.

1.4.2 MRI sequences

The pulse sequences allow to create images where the tissues are properly characterized by T1, T2, ρ typical values of the measured signal FID. These pulse sequences permit to empathize the dependence of the measured signal (FID) from one of these three parameters.
The parameters that influence the result of the image are:

- the **Repetition Time** (TR), which expresses the time interval between the beginning of a sequence and the beginning of the next;

- the **Echo Time** (TE), which is the time between the RF pulse and the centre of echo,that is the instant in which the signal acquires maximum amplitude. The amplitude of the transversal magnetization M_{xy} at the echo peak depends on T_E and T_2 of the tissue. In fact, for a same type of tissue, for T_E short it have that the component M_{xy} is reduced by an amount related to T_2 of the tissue and so the echo signal acquired will have an intensity determinate by the T_E chosen. The choice of T_E is very important since it provides the contrast of the image.

- the **Flip Angle** (FA), which is the angle $\alpha = \gamma B_1 t$ between the direction of $\vec{B_0}$ field and magnetization vector $\vec{M}$. As can be seen from the formula, a high value of FA is achieved with a longer

duration of activation of the RF pulse or grater intensity of the $\vec{B_1}$. For this reason, when it is necessary to acquired images very quickly to monitor phenomena of short duration it tries to fix FA values rather low.

Through the combination of TR and TE (long or short), T1-weighted, T2-weighted or DP-weighted images are obtained. A few examples of basic sequences are described in the following:

- **TSE** (Turbo Spin Echo) is a multi-echo spin-echo sequence where multiple lines of k-space are recorded in a single excitation by different spin-echoes. Unlikely the traditional spin-echo sequence, which captures a single line of k-space and then it is necessary to wait until the magnetization state of equilibrium returns (usually a few seconds), a TSE sequence acquires a series of echoes produced by various impulses at 180° that refocused the magnetization after the 90° pulse excitation (Figure 1.8) For each of these echoes is assigned a different phase encoding and then fills a different line of K-space. The phase encoding is carried out by applying a gradient along the axis of the stage before the formation of the echo. The same gradient is then reapplied immediately reversed after the echo. In this way, the spins realign and behave as if they had never been disturbed in the echo later. The number of recordable echo (*echo train length* or ETL) for each signal varies from 2 to over 30, depending largely on the length of the sequence repetition time (TR) and by the type of scanner used; the greater will be the TR of many more echo sequence can be registered for each signal. The quality, such as the amplitude of the signal collected at each subsequent refocusing, will always be less because

it will be subject to decay T2 but still useful to the formation of the image. Typical values of ETL for T1-weighted sequences are 2-3 (as it is necessary a short TR) whereas for T2-weighted sequences, given the considerable length of the TR, the train of echoes can reach considerable values even up to over 30. Since the image contrast is given mainly from the centre of k-space, it may change by deciding to acquire the same between the first echoes, or after a certain time. Later it acquires the centre of k-space the greater will be the attenuation suffered from it for the relaxation time T2, and thus the image will be more T2 weighted; if the centre is acquired among the first echoes, the sequence will become T1-weighted or proton density-weighted according to the second TR. Thus, being particularly fast, TSE sequences are adopted for morphological images. Since some tissues and pathologies have similar T1 values but different T2 values, it is advantageous to have an imaging sequence which produces images with a T2 dependence.

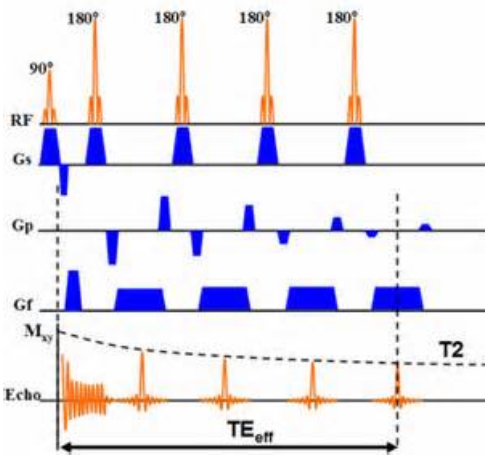

Figure 1.8: TSE sequence

- **EPI** (echo planar image) sequences allow to have similar contrast to the sequences Spin-Echo and Gradient-Echo with a significant reduction in the time of acquisition. The peculiarity of the EPI technique (Figure 1.9) is the possibility to have an image in a few periods T_R: in fact, for each period of repetition is applied a frequency encoding gradient in rapidly oscillating between positive and negative polarity, which allows to obtain the formation of more subjected echo to different phase encoding gradients. The disadvantages of this technique are represented any signs of blurring (shaken and blurred image), magnetic susceptibility artefacts, distortion and a lower SNR than the other acquisition sequences previously considered. Given the minimal presence of motion artefacts and high temporal resolution, EPI is indispensable to studies both of diffusion and perfusion images in vivo.

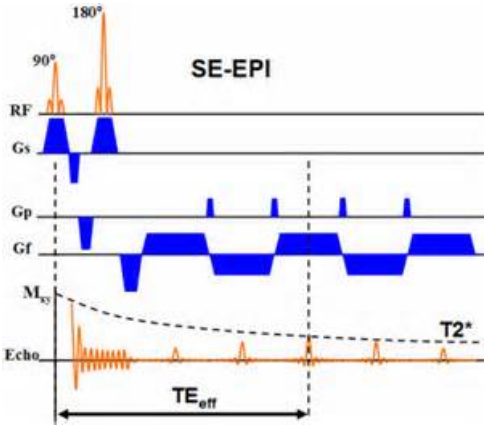

Figure 1.9: EPI sequence

- **FLASH** sequences, emerged as a gradient echo sequence which combines a low-flip angle radio-frequency excitation of the MR signal (recorded as a spatially encoded gradient echo G_x) with a

rapid repetition of the basic sequence, is shown in Figure 1.10. The repetition time is usually much shorter than the typical T1 relaxation time of the protons in biologic tissue. Only the combination of a low-flip angle excitation which leaves unused longitudinal magnetization for an immediate next excitation with the acquisition of a gradient echo which does not need a further radio-frequency pulse that would affect the residual longitudinal magnetization, allows for the rapid repetition of the basic sequence interval and the resulting speed of the entire image acquisition. FLASH reduces the typical sequence interval to what is minimally required for imaging: a slice-selective radio-frequency pulse and gradient, a phase-encoding gradient, and a (reversed) frequency-encoding gradient generating the echo for data acquisition.
For radial data sampling, the phase and frequency-encoding gradients are replaced by two simultaneously applied frequency-encoding gradients that rotate the Fourier lines in data space.
In fact, gradient-echo represents an evolution of the spin-echo sequence in terms of reduced acquisition times and clinical utility. The advantages of the sequence Gradient Echo consist in the reduction of the acquisition time with greater facility using the gradients respect to radio frequency pulses and in least loss of energy to the patient; for all this it must be added the ability to visualize vascular structures with high signal. The contrast and the weighing of the images obtained with this sequence depends on T_E, T_R and flip angle. Choosing suitably parameters in the sequence T1, T2, T2* and proton density weighted images with a wide variation of contrast can be had.

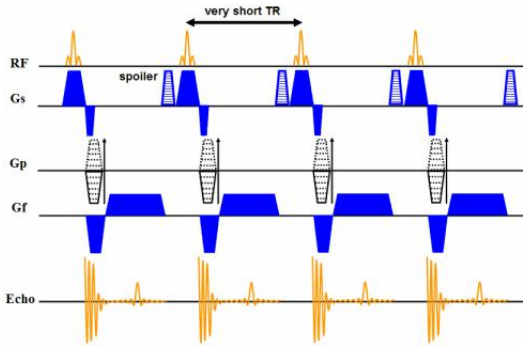

Figure 1.10: GE sequence

1.4.3 Instrumentation

At first view, an image of resonance is similar to an image obtained by computed tomography (CT). Externally the equipment for a CT and for a resonance are often similar; the main difference is the length of the tube which is inserted in the patient, which is smaller in the case of CT than MR. In both the patient lying on a motorized table is inserted into a ring. A commercial scanner (Figure 1.11) is mainly formed by elements that create static magnetic fields or variable in time and space, coordinated by a complex control electronics. These elements are:

- the main magnet, whose function is to create a static magnetic field and homogeneous $\vec{B_0}$ with high intensity to allow the polarization of the nuclei. Can be used permanent, resistive or superconducting magnets and the intensity of the magnetic field can also be distinguished in : high field ($\geq$ 1.5T); medium field (0.5-1T), low-field ($\leq$ 0.5T);
- the radio frequency coils, which generate the rotating magnetic field $\vec{B_1}$ at the Larmor frequency;

- the antenna detects the RF energy from the field $\vec{B}_1$. Sometimes can be double (one for the issue and one for the reception) or single (both issuers and receivers);
- the gradient coils, which generate magnetic fields that vary linearly in space, which are essential to the generation of images;
- various auxiliary coils, which are used to compensate for any unevenness or to otherwise modify the geometry of the main areas.

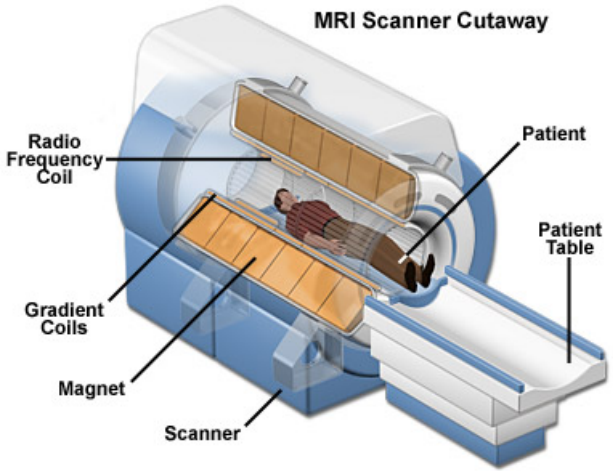

Figure 1.11: MRI scanner. The average time of an examination varies from 10 to 35 minutes (or 30-60 min for total body), during this time are produced dozens of images of the body.

1.4.4 Diffusion study using MRI: Diffusion Weighted Images

The diffusion-weighted imaging (DWI) is a magnetic resonance technique sensitive to the diffusive properties of water molecules and it is presented as an important tool for the clinical diagnosis [7]. This technique allows to obtain images in which the signal intensity is related to the random Brownian movement of water molecules (diffusion) in the presence of a strong magnetic gradient. This causes a loss of signal in RM as a result of the consistency de-phasing of the spins. The application of a pair of strong gradients capable of enhancing the differences of diffusion of water molecules in biological tissues is known as sensitization to diffusion or diffusion-weighted image. The principle of proton diffusion, in fact, is based on the observation that in a stationary system of nuclei not in balance, subject to a magnetic field gradient, the spins undergo a diffusive flux. The density of this flux depends on the gradient of the magnetic field according to the diffusion coefficient (D) typical of the system, such as a coefficient which measures the degree of translation of the water molecules over small distances related to Brownian movements, for each volume element (voxel) of an image. These distances are typically microscopic (of the same order of magnitude of cell size) so the measurement of the proton diffusion may allow to evaluate the integrity and cellular capabilities in both normal and pathological conditions. In fact, the interactions between the intracellular and extracellular environment affect the diffusion of water molecules resulting in disturbance of their diffusive flux. The analysis of the relaxation times and the study of proton diffusion with MR allow to obtain different information about the state of the protons

in biological tissues, especially the water “bound” and “free” [2] [43]. Water molecules can present two kinds of movement: "coherent" and "incoherent". The first is marked by the movement of water molecules along a certain axis, such as the bloodstream. The motion "incoherent" (for example, the thermal Brownian motion) is characterized by the possible displacement of water molecules along each arbitrary axis in the space. The distinction between these two types of movement is sometimes difficult: in fact, in a voxel, where there are many blood vessels (each of which characterized by coherent motion), the analysis of the water movement as a whole may appear inconsistent.
As previously said in the paragraph 1.4.1, from an experimental point of view the application of a field gradient along an axis (for example z) creates a de-phasing of the magnetic moment of the spin, which is a function of its position along the z axis [22]. The reduction of the magnetization is proportional to the intensity of the gradient G and the time of application of gradient δ, which must be small because otherwise the diffusion during the application of the gradient would no longer be negligible. To make the images more susceptible to this phenomenon, two powerful additional gradients that are placed symmetrically with respect to the impulse to 180° are applied and varying the amplitude of these gradients it is possible to get a different weighing of the images in diffusion. The degree of weighting diffusion is described by b_value [34], a parameter that is determined by the pattern of the gradients used in the experiment of MR:

$$b\_value = (\gamma G \delta)^2 (\Delta - \tfrac{\delta}{3}) \tag{1.13}$$

where δ and G are respectively the duration and the intensity of the gradient pulses, and Δ is the time interval between the two gradient pulses.

The scheme most commonly implemented for DWI is that of a gradient bipolar Stejskal-Tanner [27]: the diffusion sequence has an additional set of gradient pulses referred as G_D.

The G_D pulse is applied along the x, y, or z direction to obtain images of diffusion in the x, y, or z directions respectively. These two G_D pulses are identical in amplitude and width (δ), separated by a time Δ, and placed symmetrically about the 180°pulse.

The function of the G_D pulses is to de-phase magnetization from spins which have diffused to a new location in the period Δ.

These pulses have no effect on stationary spins. For example, a stationary spin exposed to the first G_D pulse, applied along the z axis, will acquire a phase in radians given by $\varphi = 2\pi\gamma \int_z G_z \, dt$.

The spin will acquire an equal but opposite phase from the second pulse since the pulses are on different sides of the 180° RF pulse.

The relationship between the signal (S) obtained in the presence of a G_D in the z direction (G_z) and the diffusion coefficient in the same direction (D_z) is given by the following equation:

$$\mathrm{S} = S_0 e^{-[(\gamma G_z \delta)^2 D_z (\Delta - \frac{\delta}{3})]} \tag{1.14}$$

where S_0 is the signal at G_z=0 and D_z is a scalar value called apparent diffusion coefficient (ADC).

Applying the b_value equation 1.13, the equation 1.14 may be written in a simpler form:

$$S_i = S_0 e^{-b_i ADC} \tag{1.15}$$

where S_i is the signal intensity measured on the i-th b_value image and b_i is the corresponding b_value. If the gradients Stejskal-Tanner are applied to a conventional sequence, in the duration of acquisition of each image of diffusion could fit heavy artefacts along the direction of the phase encoding of the signal, which would make it almost impossible to evaluate the diffusion coefficient. These problems can be partially overcome by using excitation sequences rapid ECO-Planar [paragraph 1.4.2] with gradient pulses "weighted " in diffusion. The EPI technique uses large and fast gradients reading to generate a complete set of echoes of the gradient, and is extremely sensitive to the proton diffusion, although it is still subject to distortion and have a low spatial resolution. This set of echoes can be realized both in a spin-echo sequence, where a pair of gradient pulses of the same polarity are applied to both sides of a 180 ° pulse, that in a sequence in the gradient echo (Ge), where a pair of bipolar gradient is applied before the acquisition of the signal. The DWI with EPI image can produce an excellent contrast to noise ratio (CNR), because the signal of most organs is very low while that of injury is high. In tumours, the DWI with a b value intermediate (eg $500\frac{s}{mm^2}$) shows a high intensity. Since the intensity of the signal in DWI can be influenced by the intensity of the signal in T2-weighted images, the high intensity of the tissues in T2 can manifest as an increase in signal intensity in DWI (effect

T2 shine through). Therefore, the DWI with a higher of b_value (eg 800-1000 $\frac{s}{mm^2}$) may be necessary for the study of the pelvis. Since the diffusion processes in biological tissues are very complex, it is well to remember to introduce a new diffusion parameters known as apparent diffusion coefficient (ADC): it is a measurement of molecular diffusion that reflects the presence of restrictions, such as viscosity and spatial barriers. The changes in ADC values appear to occur before that the morphological changes become apparent, playing an important role in the characterization of tissue in vivo (as tumours) and in monitoring response to treatment [2] [43]. The ADC maps can be obtained by acquiring two DWI in different b_value and using the relation:

$$\text{ADC} = \frac{1}{(b1-b2)} \ln(\frac{S2}{S1}) \tag{1.16}$$

where (b1, b2) and (S1, S2) are respectively the b_value and the signals of the two DWI [28] [4]. Qualitatively, the ADC maps appear as a negative DWI, which instead appears hypo-intense. The ADC, besides depending strongly on the cell density, is related to the degree of malignancy of tumours, in which the high degree shows a low value of the ADC, and then provides information on cellularity and tumour aggressiveness. The ADC maps, in post-therapy monitoring phase, are able to view and detect the presence of recurrence and allow to differentiate the viable tumour tissue from necrosis, characterized by an increase of the diffusivity of water molecules. Their are obtained acquiring a set of diffusion images that are processed by software: to each pixel of the image is associated an ADC value of the voxel corresponding of

the acquired slice. It is also possible to discriminate the tumour cystic component from the solid: the cystic component has a high value of diffusivity and then a low signal; so, the ADC maps are not affected by any residual weighing T2 and contain a precise quantitative information related to diffusion processes but its main limitation, as DWI, is the dependence on the direction of the applied gradient of diffusion.

Parametric map estimation

DWI images through the ADC can reveal the water movement freedom in extracellular space of the district. The multi ADC map had a key role in this work: in fact, as it has been just mentioned, the changes in ADC values appear to occur before that the morphological changes become apparent, playing an important role in the characterization of tissue in vivo and in monitoring response to treatment [1]. It is expected that high values of ADC are presented in the patients after the treatment. Therefore, the ADC map was used to determine the interaction between ADC and dose values absorbed by the patient. The name "multi" refers to ADC map computation: the map was the result of a routine previously implemented whose inputs are the concatenation of all final DWI merged volumes and a vector containing b_values (0, 150, 800, 1000) [32].

Chapter 2

Experimental protocol

This work is a collaborative research between Department of Electronic, Information and Bioengineering at the Politecnico di Milano and the Laboratory of Advanced Radiologic Analysis (LARA) at Department of Diagnostic Imaging and Radiotherapy of the Fondazione IRCCS Istituto Nazionale dei Tumori of Milan.

2.1 Patients

In this study, five patients have been enrolled with histological diagnosis of malignant prostate tumours [1] (from 64 to 75 years old).
All the patients undergone to radiotherapy treatment, as reported in Table 2.1.

[1] In this contest, the degree of tumour is classified as *T1c* for the tumour identified by needle biopsy (eg, because of elevated PSA-Prostate Specific Antigen) while as *T2b* for the tumour confined to the prostate that involves more than half of one lobe but not both lobes.

Table 2.1: Classification and cataloguing of the data provided by the hospital database.

Patient	Pt1	Pt2	Pt3	Pt4	Pt5
Patient ID	3127039	3133919	3116610	9102802	3135618
Age (years)	75	73	65	72	54
Degree of Tumour	T2b	T2b	T1c	T1c	T1c
Date and type of exam	21/02/2012 (MR)	06/03/2012 (MR)	28/02/2012 (MR)	16/02/2012 (MR)	03/04/2012 (MR)
	21/02/2012 (CT)	06/03/2012 (CT)	28/02/2012 (CT)	16/02/2012 (CT)	03/04/2012 (CT)
	08/05/2012 (MR)	26/07/2012 (MR)	17/07/2012 (MR)	15/05/2012 (MR)	05/07/2012 (MR)
Treatment	RapidARC	RapidARC	RapidARC	RapidARC	RapidARC
Prescribed dose (Gy)	78	78	78	78	65

2.2 Imaging protocol

We analysed Magnetic Resonance Images (MRI) acquired at Istituto Nazionale dei Tumori (INT) in Milan, with a Philips scanner of 1.5 T. For each patient, two subsequent exams have been considered: a pre and post treatment (usually after 3 months). Each exam included morphological and functional sequences with relative parameters:

- T1 turbo spin echo (TSE) images pre and post contrast with TR 564 ms, TE 12 ms, resolution 0.68 x 0.68 x 1 mm, slice thickness 3 mm and gap 0.3 mm, field of view (FOV) 240 x 197 mm;
- T2 turbo spin echo (TSE) images pre contrast with TR 4000 ms, TE 120 ms, resolution 0.45 x 0.45 x 1 mm, slice thickness 3 mm and gap 0.3 mm, FOV 160 x 125 mm;
- Diffusion weighted image (DWI) based on echo planar imaging sequence, using 4 b_values (0, 150, 800, 1000 s/mm^2), with TR 8585 ms, TE 66.4 ms, resolution 1.38 x 1.38 x 1 mm, slice thickness 3 mm and gap 0.3 mm, FOV 165 x 157 mm.

These parameters are also reported in Table 2.2.

Table 2.2: Parameters relating to the morphological and functional sequences.

Sequences	Type	TR	TE	Resolution	Slice thickness	gap	FOV
T1 pre Gd-contrast	TSE	564 ms	12 ms	0.68x0.68x1 mm	3 mm	0.3 mm	240 x 197 mm
T1 post Gd-contrast	TSE	564 ms	12 ms	0.68x0.68x1 mm	3 mm	0.3 mm	240 x 197 mm
T2 pre Gd-contrast	TSE	4000 ms	120 ms	0.45x0.45x1 mm	3 mm	0.3 mm	160 x 125 mm
DWI_b0	EPI	8585 ms	66.4 ms	1.38x1.38x1 mm	3 mm	0.3 mm	165 x 157 mm
DWI_b150	EPI	8585 ms	66.4 ms	1.38x1.38x1 mm	3 mm	0.3 mm	165 x 157 mm
DWI_b800	EPI	8585 ms	66.4 ms	1.38x1.38x1 mm	3 mm	0.3 mm	165 x 157 mm
DWI_b1000	EPI	8585 ms	66.4 ms	1.38x1.38x1 mm	3 mm	0.3 mm	165 x 157 mm

In addition, we analysed Computer Tomography (CT) images acquired on a Philips CT scanner dedicated to radiotherapy treatment planning [2] and three dose images, related to the quantity of received radiation, for each patient.

2.3 Software and resources

All MR and CT, originally stored as DICOM (Digital Imaging and Communications in Medicine) format, images are transformed in NIFTI (Neuroimaging Informatics Technology Initiative) format, that is useful for further processing.
For a correct visualization and manipulation of data, two open source viewers of medical images are used: MRIcro and Irtk.

MRIcro

MRIcro [15] is a Windows or Linux utility built specifically for opening and analyzing medical images. Generally, MRIcro allows efficient viewing and exporting of brain images, but it can be used for other

[2] In this contest, *RapidArc* radiotherapy technology was used. It is a new form of image-guided, intensity-modulated radiation therapy (IMRT). Using RapidArc technology, clinicians can deliver a precise radiation dose that conforms to the shape of the tumour, while limiting the amount of radiation that reaches surrounding healthy tissues. A RapidArc treatment is delivered with a single 360-degree rotation of the linear accelerator, which takes less than two minutes.

parts of the body (as in this study, the prostate).
It is a standalone program, but includes also drawing tools to complement SPM (Statistical Parametric Mapping, a software that allows neuro radiologist to analyse MRI, fMRI and PET images) or calculate the volume of the lesion, allows to identify 3D regions of interest (ROIs) and can create analyze format headers (such as HDR, NII, CUB, HEAD, PNG, BMP, TIF, or JPEG) for exporting images to other platforms.
Moreover, the application allows users to view a histogram, adjust the color scheme, overlap multiple regions of interest, rotate images to match the SPM template images. An example of visual interface of this software is shown in Figure 2.1.

IRTK

IRTK (Image Registration Toolkit) is a software developed for research purposes only, and hence should not be used as a diagnostic tool. It provides executables of different categories: image registration, landmark registration, surface registration, transforming images and points, transformation and general image processing [16].
An example of visual interface of this software is shown in Figure 2.2.

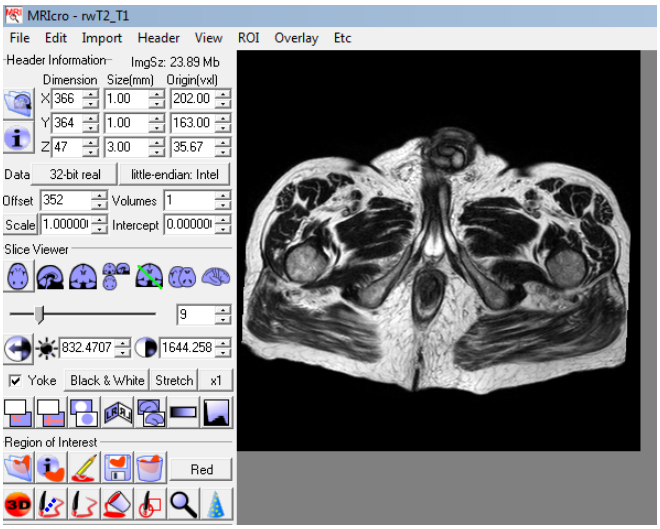

Figure 2.1: An example of MRIcro visual interface. At the left of the window, there are all the available commands: header informations, viewer slice (transverse, sagittal and coronal) and region of interest.

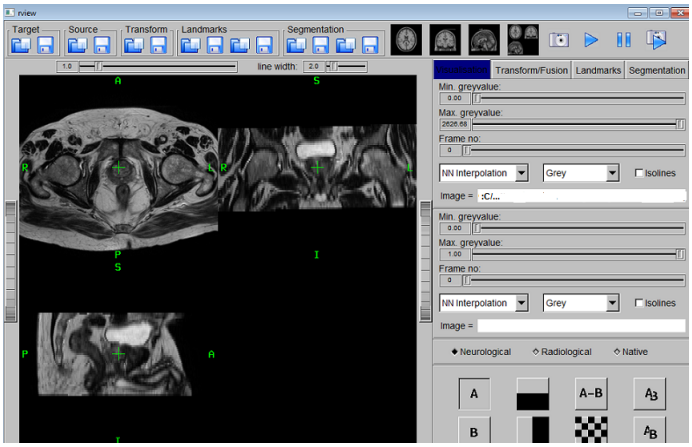

Figure 2.2: An example of IRTK visual interface. At the left of the window, different slice viewers show the same image in three different planes.

Chapter 3

Image Registration

3.1 Introduction

Registration is the determination of a geometrical transformation that aligns points in one view of an object with corresponding points in another view of that object or of another object [36]. This concept is schematically represented in Figure 3.1.

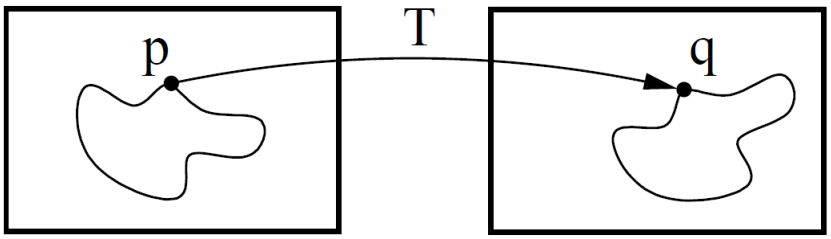

Figure 3.1: Image registration is the task of finding a spatial transform mapping on image into another.

Three-dimensional images are acquired by tomographic modalities, such as computed tomography (CT), magnetic resonance (MR) imaging, single-photon emission computed tomography (SPECT), and positron emission tomography (PET). In each of these modalities, a contiguous

set of two-dimensional slices provides a three-dimensional array of image intensity values. Typical two-dimensional images may be x-ray projections captured on film as a digital radiography or projections of visible light captured as a photograph or a video frame. From an operational view, the inputs of registration are the two views to be registered; the output is a geometrical transformation, which is merely a mathematical mapping from points in one view to points in the second. If the corresponding points are mapped together, the registration is successful. In ITK, registration is performed within a framework of pluggable components that can easily be interchanged [42]. This flexibility means that a combinatorial variety of registration methods can be created, allowing users to pick and choose the right tools for their specific application.

Registration Framework The components of the registration framework and their interconnections are shown in Figure 3.2.

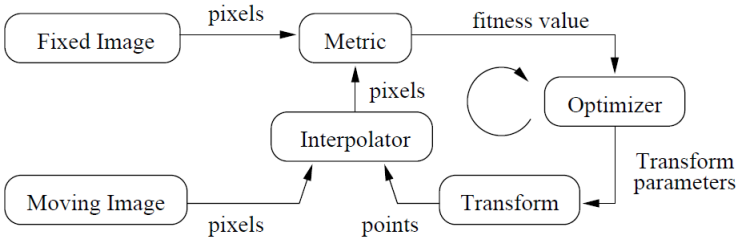

Figure 3.2: The basic components of the registration framework are: two input images, a transform, a metric, an interpolator and an optimizer.

Firstly the input of the registration process are two images: one is defined as the fixed image $f(X)$ and the other as the moving image $m(X)$. Where X represents a position in N-dimensional space.

Registration is treated as an optimization problem with the goal of finding the spatial mapping that will bring the moving image into alignment with the fixed image. The transform component $T(X)$ represents the spatial mapping of points from the fixed image space to points in the moving image space. The interpolator is used to evaluate moving image intensities at non-grid positions. The metric component $S(f, mT)$ provides a measure of how well the fixed image is matched by the transformed moving image. This measure forms the quantitative criterion to be optimized by the optimizer over the search space defined by the parameters of the transform.

3.1.1 Metrics

In ITK, metric quantitatively measure how well the transformed moving image fits the fixed image by comparing the gray-scale intensity of the images [36]. These metrics are very flexible and can work with any transform or interpolation method and do not require reduction of the gray-scale images to sparse extracted information such as edges. The metric component is perhaps the most critical element of the registration framework. The selection of metric to use is highly dependent on the registration problem to be solved. For example, some metrics have a large capture range while others require initialization close to the optimal position. In addition, some metrics are only suitable for comparing images obtained from the same imaging modality, while others can handle inter-modality comparisons. Unfortunately, there are no clear-cut rules to choose a metric. The basic inputs to a metric are: the fixed and moving images, a transform and an interpolator. The method 'GetValue' can be used to evaluate the quantitative criterion

at the transform parameters specified in the argument. Typically, the metric samples points within a defined region of the fixed image. For each point, the corresponding moving image position is computed using the transform with the specified parameters, then the interpolator is used to compute the moving image intensity at the mapped position.

The following list shows some metrics currently available in ITK [42]:

- Mean squares
- Normalized correlation
- Mean reciprocal squared difference
- Mutual information metric
- Mutual information by Mattes
- Kullback Liebler distance metric by Kullback and Liebler
- Normalized mutual information
- Mean squares histogram
- Correlation coefficient histogram
- Cardinality Match metric
- Kappa Statistics metric
- Gradient Difference metric

In the following sections, each metric is described in detail. For ease of notation, it will refer to the fixed image $f(X)$ and transformed moving image $(mT(X))$ as images A and B.

Mean Squares Metric

The Mean Squares Metric computes the mean squared pixel-wise difference in intensity between image A and B over a user defined region:

$$MS(A, B) = \frac{1}{N} \sum_{n=1}^{N} (A_i - B_i)^2 \tag{3.1}$$

where:

A_i is the i-th pixel of Image A
B_i is the i-th pixel of Image B
N is the number of pixels considered

The optimal value of the metric is zero. Poor matches between images A and B result in large values of this metric. This metric is simple to compute and has a relatively large capture radius. This metric relies on the assumption that intensity representing the same homologous point must be the same in both images. Hence, its use is restricted to images of the same modality. Additionally, any linear changes in the intensity result in a poor match value.

Normalized Correlation Metric

The Normalized Correlation Metric computes pixel-wise cross-correlation and normalizes it by the square root of the autocorrelation of the images:

$$NC(A,B) = \frac{\sum_{n=1}^{N}(A_i * B_i)}{\sqrt{\sum_{n=1}^{N} A_i^2 * \sum_{n=1}^{N} B_i^2}} \tag{3.2}$$

where:

A_i is the i-th pixel of Image A
B_i is the i-th pixel of Image B
N is the number of pixels considered

Misalignment between the images results in small $NC(A,B)$ values. The use of this metric is limited to images obtained using the same imaging modality. The metric is insensitive to multiplicative factors between the two images. This metric produces a cost function with sharp peaks and well defined minima. On the other hand, it has a relatively small capture radius.

Mean Reciprocal Square Differences

The Mean Reciprocal Square Differences metric computes pixel-wise differences and adds them after passing them through a bell-shaped function $\frac{1}{1+x^2}$

$$PI(A,B) = \sum_{i=1}^{N} \frac{1}{1+\frac{(A_i+B_i)^2}{\lambda^2}} \tag{3.3}$$

where:

A_i is the i-th pixel of Image A

B_i is the i-th pixel of Image B

N is the number of pixels considered

λ controls the capture radius

The optimal value is N and poor matches results in small measure values. This image metric has the advantage of producing poor values when few pixels are considered. This makes it consistent when its computation is subjected to the size of the overlap region between the images. The capture radius of the metric can be regulated with the parameter λ. The profile of this metric is very peaky. The sharp peaks of the metric help to measure spatial misalignment with high precision. The notion of capture radius is used here in terms of the intensity domain, not the spatial domain. In that regard, λ should be given in intensity units and be associated with the differences in intensity that will make drop the metric by 50%. The metric is limited to images of the same image modality. The fact that its derivative is large at the central peak is a problem for some optimizers that rely on the derivative to decrease as the extrema are reached. This metric is also sensitive to linear changes in intensity.

Mutual Information Metric

This metric computes the mutual information (MI) between image A and image B. Mutual information measures how much information one random variable (image intensity in one image) tells about another random variable (image intensity in the other image). The major advantage of using MI is that the actual form of the dependency does not have to be specified. Therefore, complex mapping between two images

can be model. This flexibility makes MI well suited as a criterion of multi-modality registration. Mutual information is defined in terms of entropy.

$$H(A) = -\int p_A(a) \log p_A(a) da \tag{3.4}$$

be the entropy of random variable A, H(B) the entropy of random variable B and

$$H(A, B) = -\int p_{AB}(a, b) \log p_{AB}(a, b) da db \tag{3.5}$$

Let be the joint entropy of A and B. If A and B are independent, then

$$p_{AB}(a, b) = p_A(a) p_B(b) \tag{3.6}$$

and

$$H(A, B) = H(A) + H(B). \tag{3.7}$$

However, if there is any dependency, then

$$H(A, B) < H(A) + H(B).$$

(3.8)

The difference is called Mutual Information : I(A,B)

$$I(A, B) = H(A) + H(B) - H(A, B)$$

(3.9)

Mattes et al. Implementation A form of mutual information metric available in ITK follows the method specified by Mattes et al. In this implementation, only one set of intensity samples is drawn from the image. Using this set, the marginal and joint probability density function (PDF) is evaluated at discrete positions or bins uniformly spread within the dynamic range of the images. Entropy values are then computed by summing over the bins. Since the fixed image PDF does not contribute to the metric derivatives, it does not need to be smooth. Hence, a zero order (boxcar) B-spline kernel is used for computing the PDF. On the other hand, to ensure smoothness, a third order B-spline kernel is used to compute the moving image intensity PDF. The advantage of using a B-spline kernel over a Gaussian kernel is that the B-spline kernel has a finite support region. This is computationally attractive, as each intensity sample only affects a small number of bins and hence does not require a N $\times$ N loop to compute the metric value. During the PDF calculations, the image intensity values are linearly scaled to have a minimum of zero and maximum of one. This rescaling means that a fixed B-spline kernel bandwidth of one can be used to handle image data with arbitrary magnitude and dynamic range.

Normalized Mutual Information Metric

Given two images, A and B, the normalized mutual information may be computed as

$$NMI(A,B) = 1 + \frac{I(A,B)}{H(A,B)} = \frac{H(A)+H(B)}{H(A,B)} \tag{3.10}$$

where the entropy of the images are $H(A)$ and $H(B)$, the mutual information is $I(A,B)$ and the joint entropy is $H(A,B)$.

3.1.2 Optimizers

The basic input to an optimizer is a cost function object. There are two main types of optimizers in ITK. In the first type we find optimizers whose cost functions return a single value. These are the most common type of cost functions, and are known as Single Valued functions, therefore the corresponding optimizers are known as Single Valued optimizers. The second type of optimizers are characterized by cost functions that return multiple values at each evaluation. These cost functions are common in model-fitting problems and are known as Multi Valued or Multivariate functions. The corresponding optimizers are therefore called Multiple Valued optimizers in ITK.

3.1.3 Transforms

Transform encapsulate the mapping of points and vectors from an input space to an output space. If a transform is invertible, back transform methods are also provided. Currently, ITK provides a variety

of transforms from simple translation, rotation and scaling to general affine and kernel transforms. Some of the most commonly used transforms will be discussed in detail in the following paragraphs.

Translation Transform

The Translation Transform is probably the simplest yet one of the most useful transformations. It maps all points by adding a vector to them. Vector and covariant vectors remain unchanged under this transformation since they are not associated with a particular position in space. Translation is the best transform to use when starting a registration method. Before attempting to solve for rotations or scaling, it is important to overlap the anatomical objects in both images as much as possible. This is done by resolving the translational misalignment between the images. Translations also have the advantage of being fast to compute and having parameters that are easy to interpret.

Versor Rigid 3D-Transform

This transform represents a rigid rotation in 3D space followed by a 3D translation. The rotation is specified by three angles representing rotations to be applied around the X, Y and Z axis one after another. The translation part is represented by a Vector. Users can also specify the coordinates of the center of rotation.The center coordinates are not modified during the optimization performed in a registration process.

Affine Transform

The Affine Transform is one of the most popular transformations used for image registration. Its main advantage comes from the fact that

it is represented as a linear transformation. This method represents a free from deformation by providing a deformation field from the interpolation of deformations in a coarse grid.

BSpline Deformable Transform

The BSpline Deformable Transform is designed to be used for solving deformable registration problems. This transform is equivalent to generation a deformation field where a deformation vector is assigned to every point in space. The deformation vectors are computed using BSpline interpolation from the deformation values of points located in a coarse grid, that is usually referred to as the BSpline grid [5]. The BSpline Deformable Transform is not flexible enough for accounting for large rotations or shearing, or scaling differences. In order to compensate for this limitation, it provides the functionality of being composed with an arbitrary transform. This transform is known as the Bulk transform and it is applied to points before they are mapped with the displacement field. This transform do not provide functionalities for mapping vectors nor covariant vectors, only points can be mapped. The reason is that the variations of a vector under a deformable transform actually depend on the location of the vector in space. In other words, Vector only make sense as the relative position between two points.

3.1.4 Interpolators

In the registration process, the metric typically compares intensity values in the fixed image against the corresponding values in the transformed moving image. When a point is mapped from one space to

another by a transform, it will in general be mapped to a non-grid position. Therefore, interpolation is required to evaluate the image intensity at the mapped position. Figure 3.3 illustrates the mapping of the fixed image space into the moving image space.

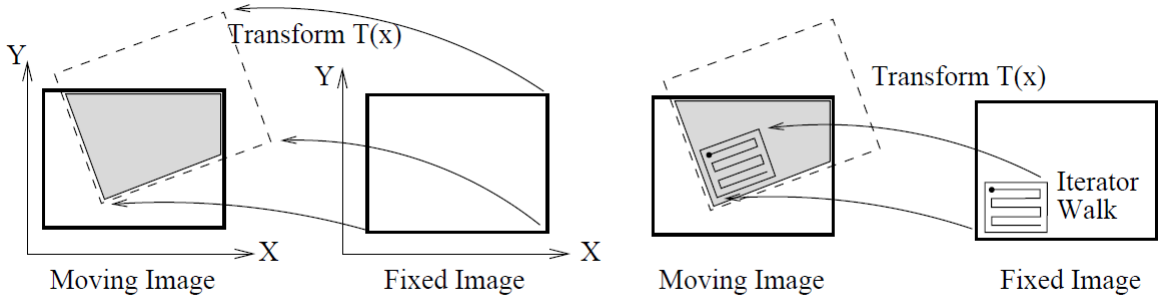

Figure 3.3: The moving image is mapped into the fixed image space under some spatial transformation. An iterator walks through the fixed image and its coordinates are mapped onto the moving image.

The transform maps points from the fixed image coordinate system onto the moving image coordinate system. The figure highlights the region of overlap between the two images after the mapping. The right side illustrates how an iterator is used to walk through a region of the fixed image. Each one of the iterator positions is mapped by the transform onto the moving image space in order to find the homologous pixel. Figure 3.4 presents a detailed view of the mapping from the fixed image to the moving image.

In general, the grid positions of the fixed image will not be mapped onto grid positions of the moving image. Interpolation is needed for estimating the intensity of the moving image at these non-grid positions. The service is provided in ITK by interpolator classes that can

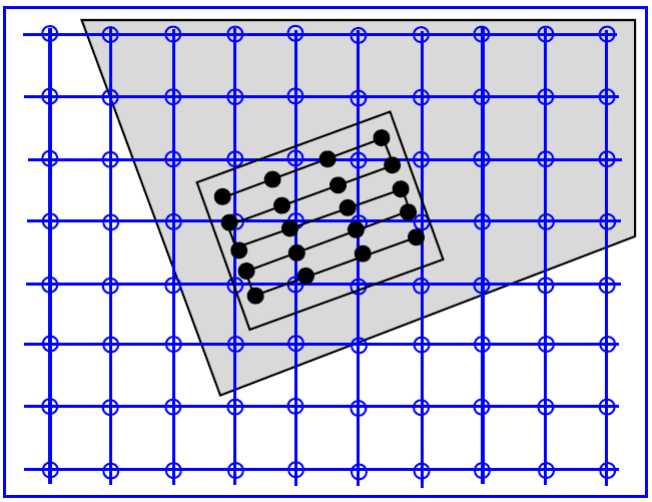

Figure 3.4: Grid positions of the fixed image map to non-grid positions of the moving image.

be plugged into the registration method. The interpolators available in ITK [36] are the following:

- Nearest Neighbour Interpolate Image Function
- Linear Interpolate Image Function
- BSpline Interpolate Image Function
- Windowed Sinc Interpolate Image Function

3.2 Implementation of the registration procedure

To evaluate functional variations in tissues due to RT, patients underwent two MRI scans concerning morphological and functional sequences, a first one before the RT and a second one at the end of the treatment [paragraph 2.2]. Therefore three registrations were computed, an intra-exam fusion (between DWI and morphological T1 PRE image) and two inter-exam: one for the registration of the post-treatment on the pre-treatment and the second for the placing of the CT on the morphological PRE image (Figure 3.5) [32].

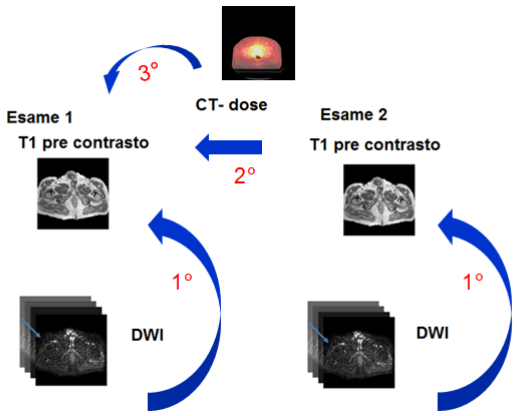

Figure 3.5: Scheme of three registrations.

The former accounts for voluntary and involuntary movements of the patient during the exam session, the latter accounts both for the tissues changing due to therapy and macro changes during the scans. Each registration was divided in two parts. In the first one a translation [paragraph 3.1.3], an affine [paragraph 3.1.3] transformation were performed in order to account the macro movement of the patient during the scan (for example the breath and the heart bit). In the second part a local non-rigid free form deformation based on b-spline [paragraph

3.1.3] was estimated. Before registration started, DICOM files had been converted in Nifti Image file format (NII). The file.nii includes an header containing information about voxel's resolution, position, orientation, image depth etc., and the image itself. The Nifti Image format has standard definition, representing 3D or 4D volumes, in grayscale or RGB space. Image registration steps were performed by Plastimatch [37][14], supervised and scheduled by MatLab [18].

3.2.1 Intra-exam registration

T1 PRE image was chosen as the reference image because of its high native resolution and the lowest b-value DWI was used as the moving image. The global transformation was based on Mattes mutual information metric, computed using 64 bins and optimized with regular-step gradient (RSG) [paragraph 3.1.2]; instead the local deformation was obtained using Mattes mutual information [paragraph 3.1.1], LBFGS optimization [paragraph 3.1.2] and 0.4 as a value for the regularization lambda. The output vector field was then applied to the remaining b-value DWIs. That was possible because all diffusion weighted images were automatically aligned by the Magnetic Resonance machine.
We visualized the result with IRTK (Figure 3.6) [paragraph 2.3] .

3.2.2 Morphological inter-exam registration

To align POST on PRE image we used the morphological POST image as moving image and the morphological PRE as the fixed one. Implementation was based on Mattes mutual Metric information, computed using 64 bins, regular-step gradient (RSG) for the rigid registration optimization and LBFGS for the non-rigid one. By applying the esti-

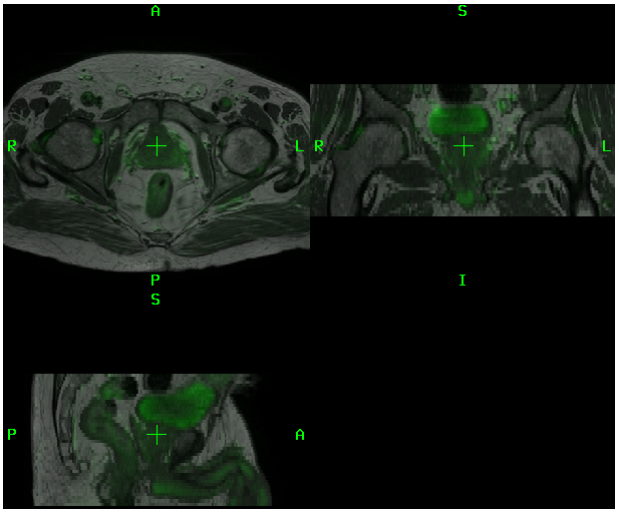

Figure 3.6: DWI registration.

mated global and local deformation field it was possible to superimpose the DWI post therapy images on the T1 PRE (Figure 3.7).

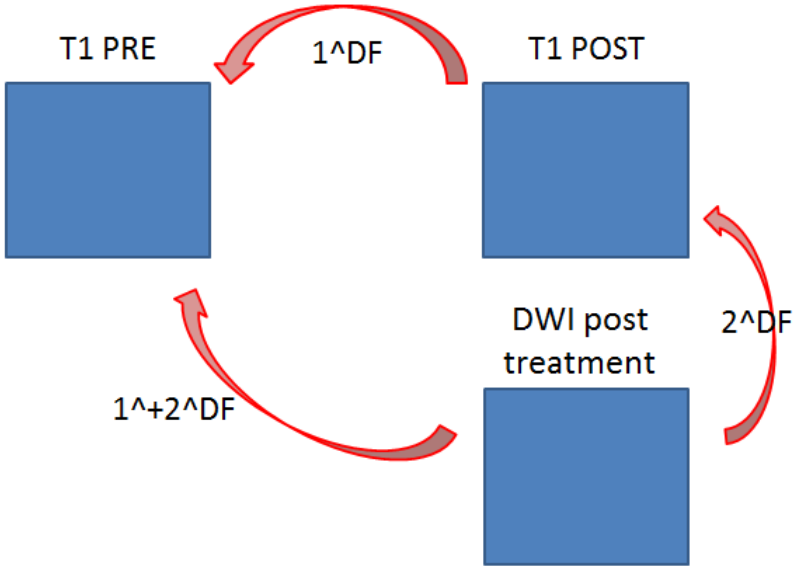

Figure 3.7: DF combination.

We visualized the result with IRTK (Figure 3.8).

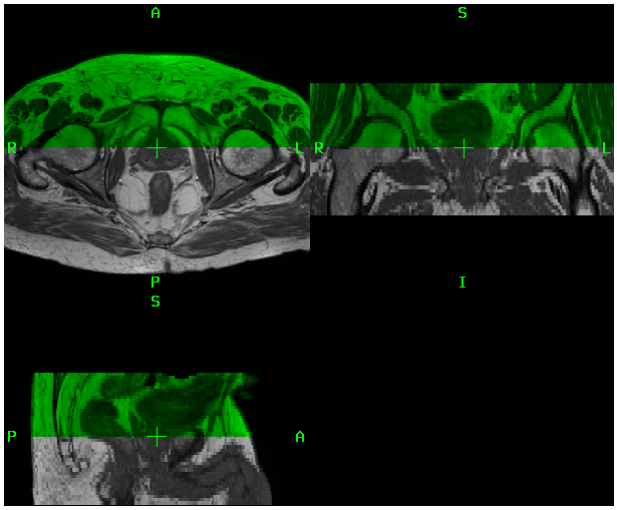

Figure 3.8: Inter-exam registration.

Table 3.1: Registration parameters.

Deformation	**Rigid**	**Non rigid**
Metric	Mattes Mutual Information	Mattes Mutual Information
Optimization	RSG	LBFGS
Transformation	Translation, Affine	B-spline

3.2.3 CT inter-exam registration

We implemented the second inter-exam registration using the PRE image as the reference and the CT as the moving. Implementation was based on Means Square Error Metric [paragraph 3.1.1], regular-step gradient (RSG) for the rigid registration optimization and LBFGS for the non-rigid one. For the local deformation regularization lambda was set to 0.4 and multi-step to 2. The vector field in output allowed to overlap the dose images on the PRE one. We visualized the result with IRTK (Figure 3.9). All parameters used in the three registrations are reported in table 3.1. Combining the VF obtained from the intra-exam registration with the VF from the inter-exam fusion, we could reported the DWIs post RT on the T1 PRE RT one.

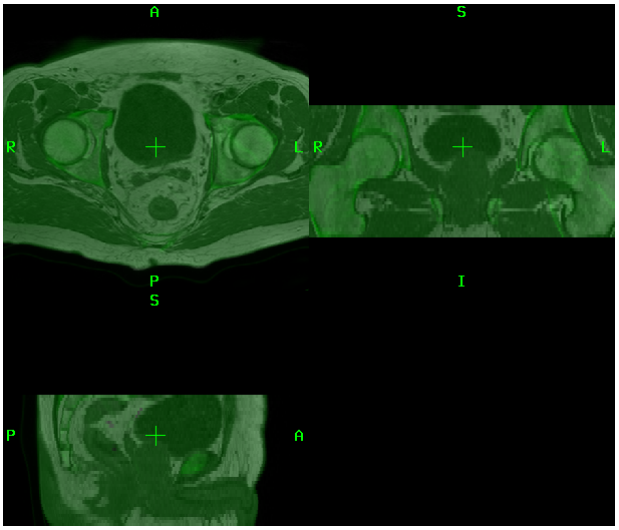

Figure 3.9: CT registration.

3.3 Validation of the registration procedure

The goal of the fusion is determining the correspondence of features between moving and fixed images. Validation is a very important post-step in registration algorithm, developed to quantify the error committed in the registration procedure. As we explained in the previous section 3.2, registration concerns of a rigid and a non - rigid deformations. The application of the non rigid B-spline transform [paragraph 3.1.3] guarantees a better result, rather than using the only translation deformation [paragraph 3.1.3]. In order to verify this assertion and proof the accuracy of our fusion methods, we implemented three validation procedures (one for each type of registration). For all three validations, the first step was the segmentation of an anatomic area in an equal number of slices. Then, we selected a reference ROI and a moving one. We applied the deformation computed during the registration steps to the ROI defined on the moving image. After that, we

computed the percentage of pixel relying on the ROI defined on the target one. In this validation, we considered the bladder as a suitable anatomic area, because it was clearly visible in morphological T1 PRE image, as well as in diffusion weighted and CT images. We achieved the manual segmentation with MRIcro software [paragraph 2.3].

Intra-exam registration validation

An expert radiologist drew ROI on bladder in the T1 image and in b_0 DWI. After that, we warped the b_0 ROI in order to obtain a superimposition of the moving ROI on the region of interest, defined on the morphological one (Figure 3.10).

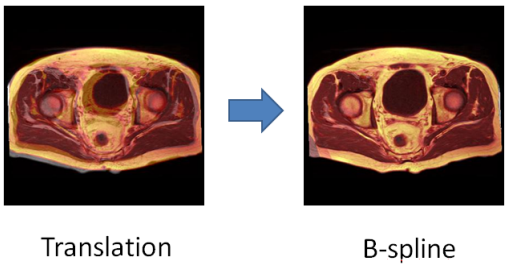

Figure 3.10: Intra-exam registration.

In order to quantify the alignment between the deformed ROI and the reference one, we computed the number of the common voxels in two ROIs and we divided the result to the number of the voxels of the reference ROI. We reported the results in two box-plots: the first corresponds to the ROI deformed using the vector field obtained after the rigid translation step; the second is obtained applying the vector field from the complete registration (Figure 3.11). The aim of this figure is to underline how different is the accuracy in the two cases.
The median of the values after the rigid translation was 0.853, while

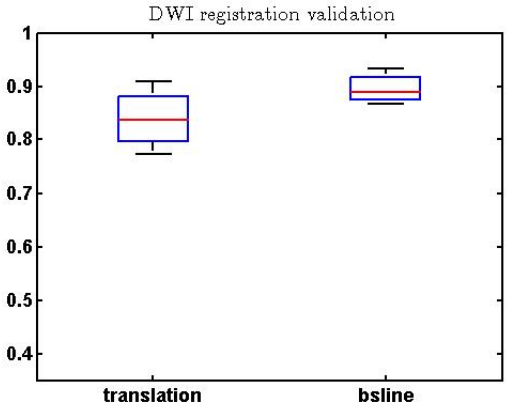

Figure 3.11: DWI registration Validation.

the median after the B-spline transform was higher, i.e. 0.958. It means that the registration algorithm performed better after the free-form deformation, rather than the translation one, as it was expected. A median value is pretty high (i.e. equal to 0.958) and indicates that the registration algorithm performed in a good way.

Morphological inter-exam registration validation

In the second registration we used the morphological T1 PRE treatment image as the fixed one and the T1 POST treatment image as the moving one. Consequently, we manually segmented the ROI on bladder in the PRE T1 image and in T1 POST image. Then we warped the T1 POST ROI on the T1 PRE ROI, with the goal to obtain an overlap of the two regions (Figure 3.12).
Even in this case, in order to quantify the alignment between the deformed ROI and the reference one, we computed the number of the common voxels in two ROIs and we divided the result to the number of the voxels of the T1 PRE ROI. We reported the results in two box-

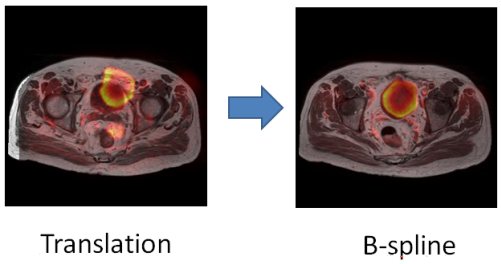

Figure 3.12: Morphological inter-exam registration.

plots: the first corresponds to the ROI deformed using the vector field obtained after the first step of fusion procedure; the second is obtained applying the DF from the complete registration (Figure 3.13).

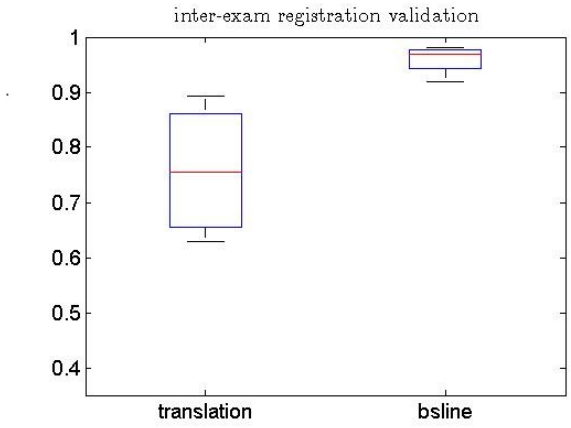

Figure 3.13: T1 PRE registration validation

The median of the values after the translation transform is 0.756, while the median after the B-spline transform is 0.984.

CT inter-exam registration validation

In the third and last registration, the reference image was the morphological T1 PRE, while the moving one was the CT. An expert radiologist drown ROI on bladder in the T1 PRE and in CT. After

that we warped the CT ROI, in order to obtain a superimposition of the moving ROI on the region of interest defined on the morphological (Figure: 3.14).

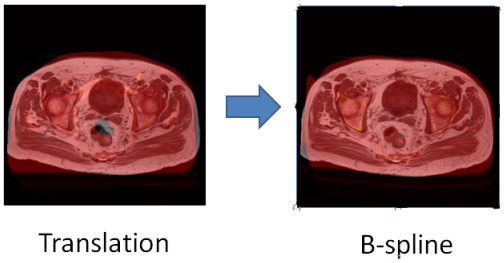

Figure 3.14: Inter-exam CT registration.

We reported the results in two box-plots: the first corresponds to the ROI deformed using the vector field in output from the translation transform; the second is obtained applying the vector field from the B-spline deformation (Figure 3.11).

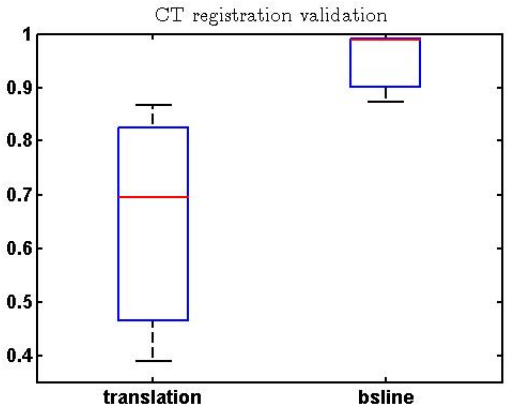

Figure 3.15: CT registration Validation.

The median of the values after the translation transform is 0.701 and after the B-spline transform is 0.998 (Figure 3.15).

3.3.1 Sensitivity and specificity

Sensitivity and specificity are statistical measures of the performance of a binary classification test, also known in statistics as classification function. Sensitivity (also called the true positive rate) relates to the test's ability to identify positive results and is calculated as:

$$Sensitivity = \frac{number\ of\ true\ positive}{number\ of\ true\ positive\ +\ number\ of\ false\ negative} \tag{3.11}$$

Specificity measures the proportion of negatives which are correctly identified and is defined as:

$$Specificity = \frac{number\ of\ true\ negative}{number\ of\ true\ negative\ +\ number\ of\ falsepositive} \tag{3.12}$$

We calculated the sensitivity and the specificity for each registration method performed. The initial step was to define the reference ROI as the ground truth and the moving one as the test. We define four areas as follow in the Figure 3.16.

- True positive (Region A): where the two ROIs are overlap;
- False positive (Region B): are the points inside the warped ROI but outside the reference one;
- False negative (Region C): are the points inside the reference ROI but outside the registered one;
- True negative (Region D): are the points outside the two ROIs.

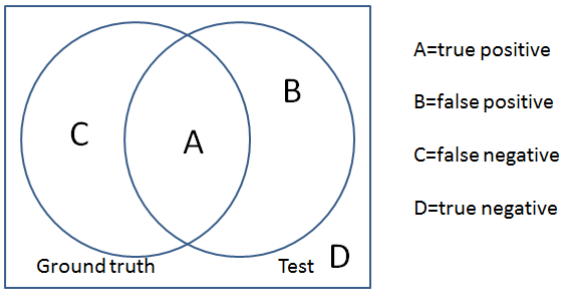

Figure 3.16: ROIs scheme.

In the following paragraphs, we described the adopted procedures to compute sensitivity and specificity for each type of registration.

Sensitivity and specificity in the three registrations

For the calculation of the sensitivity and specificity in intra-exam registration, we considered the ROI on the morphological T1 PRE as the reference and the warped region of interest segmented on the DWI as the test.
The boxes-plot underlying portrayed the obtained results (Figure 3.17).

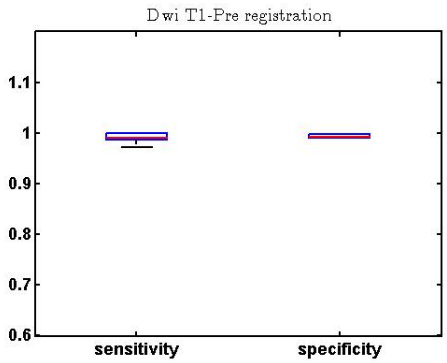

Figure 3.17: Sensitivity and specificity for the DWI intra-exam registration.

The median sensitivity and specificity are respectively 0,987 and 0,992. It means that the error committed is not high and the fixed ROI and the registered one are overlapping with a good accuracy.

The second registration consider the ROI on morphological T1 PRE treatment image as the reference and the ROI on the fused morphological T1 POST-RT image as the moving one.

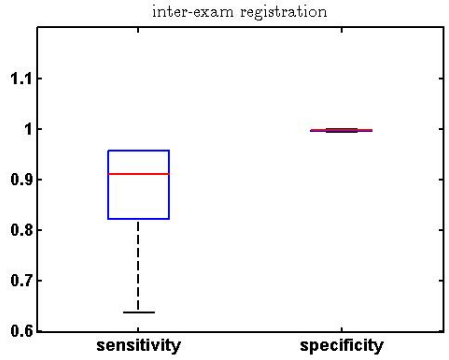

Figure 3.18: Sensitivity and specificity for morphological T1 inter-exam registration.

The median of the sensitivity values is 0.923 while the median of the specificity is 0.998 (3.18). The ROI (the bladder) was correctly registered but it's different in shape and size after RT, because of that there are too many false negatives and the sensitivity has a low value.

For the last computation, we selected the ROI on CT registered image as the test and the ROI segmented on the morphological T1 PRE image ground truth.
Once calculated sensitivity and specificity values, we could create the box plot (Figure 3.19).

The median of the values of sensitivity is near to 1 and the same result is founded for the specificity. It means that this registration algorithm is robustness and performed in a good way.

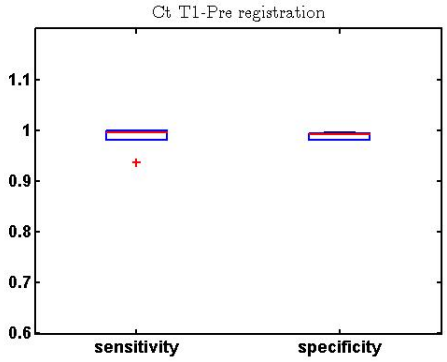

Figure 3.19: Sensitivity and specificity for CT registration.

Chapter 4

Image segmentation

Segmentation is the process of identifying and classifying data found in a digitally sampled representation using some features (grey levels, size or shape...) [36]. Typically the sampled representation is an image acquired from such medical instrumentation as CT or MRI scanners. The segmentation techniques can be divided into two classes: qualitative and quantitative methods. The first is associated with the manual segmentation while the second with semi-automatic segmentation. Regards qualitative methods, results depend strongly on the operator, the acquisition method and the manner of display window of image. Quantitative methods, however, can be further subdivided into two categories.

- **Intensity-based methods**: which used threshold or probabilistic function related to the pixels' levels of intensity. Technique like thresholding or fuzzy are part of this group.
- **Region-based methods**: based on the property in case of similarity in which the image is partitioned into regions that are similar according to a set of predefined criteria.

- **Edge-based methods**: based on the properties of gaps if instead partitioning the image on the basis of changes in the levels of grey, as the contours and edges. An example is spatial gradients of the pixels' intensity:

4.1 Fuzzy images segmentation

Image segmentation divides an image into a number of regions homogeneous, with respect to some characteristics (levels of grey, shape and size, textures, etc.). The crisp segmentation assigns to each pixel image within the region of interest probability equal to 100% (Figure 4.1).

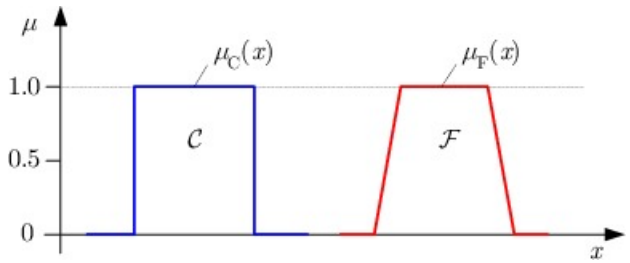

Figure 4.1: Membership functions of a crisp and a fuzzy set

Instead, in the fuzzy segmentation [9] [21] the degree of truth of the hypothesis corresponds to the degree of membership of the input value within a particular range. In fact, these ranges are not clearly separated but overlap with membership functions MF normally triangular/trapezoidal, for which each pixel image can belong to more than one region with different degrees of membership.

4.1.1 Fuzzy set

A fuzzy set is a set of elements belonging to a certain range of numbers (called *universe* U), each characterized by its degree of membership. In other words, a *fuzzy subset* A of a *ordinary set* U is defined by its *Membership Function* μ_A, which associates to each element u $\in$ U a number $\mu_A(u) \in [0,1] =$ M (called Membership Space):

$$\mu_A : U \rightarrow [0,1] \tag{4.1}$$

$\mu_A(u)$ is defined as "degree of membership of u in A". Two fuzzy sets A and B defined on the same universe set U are called *equal* if they have the same MF, that is:

$$\text{A=B} \Leftrightarrow \forall u \in U : \mu_A(u) = \mu_B(u) \tag{4.2}$$

Analogously, the fuzzy set Φ is defined *empty set* if:

$$\forall u \in U : \mu_\Phi(u) = 0 \tag{4.3}$$

Therefore, the main feature of a fuzzy set is its particular membership function, which completely defines the universe set.

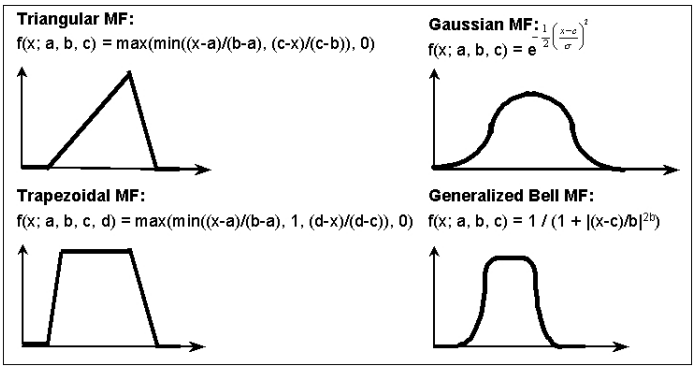

Figure 4.2: The common shapes of MF

The membership function can be of different shapes: the most common shapes of MF are shown in the Figure 4.2.
To define a membership function it is necessary to:

1. Select a variable;
2. Define the range of the variable;
3. Identify labels, which linguistically indicates that the particular set intends to represent;
4. For each label identify characteristic points;
5. Identify function shapes;
6. Check.

4.1.2 Operations between fuzzy sets

As for crisp sets, the principal operations between fuzzy sets are the union, the intersection and the complement. These operations are defined through the related MFs.

Union (logical operator OR) Given two fuzzy sets A and B of U, their union is indicated by $A \cup B$ and is also fuzzy subset of U, with membership function:

$$\mu_{A+B}(u) = \max\left(\mu_A(u), \mu_B(u)\right), u \in U \tag{4.4}$$

Thus, $A \cup B$ is represented according the relationship :

$$A \cup B = \int_U \frac{\max\left(\mu_A(u), \mu_B(u)\right)}{u} \tag{4.5}$$

Intersection (logical operator AND) Given two fuzzy sets A and B of U, their intersection is indicated by $A \cap B$ and is also fuzzy subset of U, with membership function:

$$\mu_{A*B}(u) = \min\left(\mu_A(u), \mu_B(u)\right), u \in U \tag{4.6}$$

Thus, $A \cap B$ is represented according the relationship :

$$A \cap B = \int_U \frac{\min\left(\mu_A(u), \mu_B(u)\right)}{u} \tag{4.7}$$

Complement (logical operator NOT) The complement of a fuzzy set A of U is a fuzzy set indicated by $\neg A$ and with MF:

$$\mu_{\neg A}(u) = 1 - \mu_A(u), u \in U \tag{4.8}$$

4.1.3 Fuzzy inference system

The core section of a fuzzy inference system [9] combines fuzzy membership degrees with the rule base and conducts the fuzzy reasoning process. The fuzzy inference system can be thus subdivided in the following steps:

1. **Fuzzification**: is the process of changing a real scalar value into a fuzzy value. A fuzzy subset F of a set S can be defined as a set of ordered pairs, each with the first element taken from S, and the second interval taken {0,1}. The current values of membership functions are applied to determine the degree of truth for each rule of the premise. The value 0 represents non-membership, the value of 1 indicates full membership while intermediate values represent the "degree of membership".

2. **Inference**: is the process of formulating the mapping from a given input to an output using fuzzy logic. The mapping then provides a basis from which decisions can be made. To do this, usually only MIN or PRODUCT rules are used. In the first, membership function output is "clipped" to the height of the degree of truth

calculated by the rule of the premise while in the second, the output membership function is multiplied with the degree of truth calculated of the rule of the premise. The most used solution is the first, indicated by Mamdani, which aims to get a membership function μ_R intersecting the fuzzy sets that expresses the antecedent and the consequent, using the MIN such as intersection operator [paragraph 4.1.2]. It formalizes so the knowledge related to the particular rule, regardless of what are the actual antecedents.

3. **Aggregation**: is the process by which the fuzzy sets that represent the outputs of each rule are combined into a single fuzzy set. In fact, once the membership functions have been described and the rules for a fuzzy inference system generated, the rules must be combined in some manner in order to make a decision. Aggregation only occurs once for each output variable. The input of the aggregation process is the list of truncated output functions returned by the implication process for each rule. The output of the aggregation process is one fuzzy set for each output variable.

4.2 Implementation of an automatic segmentation procedure

Aim of this part was to develop an automatic method for the identification of penile bulb. The penile bulb is a small area within the prostate and it looks like healthy tissue marginally affected during radiotherapy treatment. Data from several image techniques were available, for this reason the procedure could be defined "multidimensional". Usually, the information content inside these images is redundant. Principal Component Analysis (PCA) [paragraph 4.2.1] is the most common used data reduction technique, adopted to reduce the number of dimensions in a large number of variables problem. Penile bulb identification has been performed by means of a fuzzy approach. In order to segment automatically the penile bulb, we collected typical grey levels of the speciment from multidimensional dataset. We used different membership function [paragraph 4.2.1], which represents the probability of the pixels to be labelled bulb through voxel intensities and geometrical features. By applying these MF as a look-up table on the PRE and POST images we obtained sixteen probability maps, eight for the PRE scan and eight for the POST one. Finally for each exam, we computed a fuzzy conjunction operation by applying Mamdani minimum implication rules. At the end of this procedure we obtained two maps, one for each scan, measuring the labelling pixels probability. Then, we analysed specificity and sensitivity of the entire segmentation procedure on the selected ROI.

4.2.1 Fuzzy automatic segmentation procedure

The adopted fuzzy segmentation procedure (Figure 4.3) was composed by several blocks:

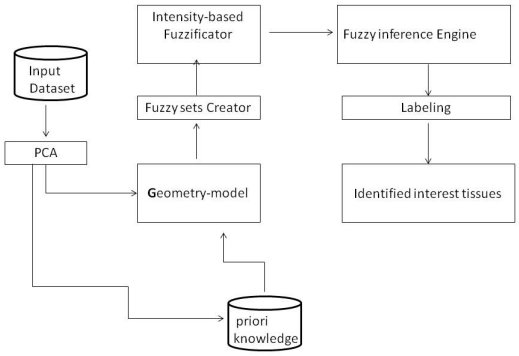

Figure 4.3: A block diagram of the fuzzy segmentation procedure.

- **principal component analysis** is used to reduce the dimensionality of the data space, suppressing data redundancy.
- **a-priori geometric knowledge** which represents a map of the most probable position of the bulb arising from anatomical knowledge.
- **geometric model** retrieves information from the whole dataset of principal components combining with the a-priori anatomical knowledge of the previous block.
- a **fuzzy sets creator** creates the fuzzy sets from the grey level distribution retrieved by the geometric model.
- a **intensity-based fuzzificator** applies the membership function computed at the previous step to the input image as a look-up table.

- a **fuzzy inference engine** is the engine decision making system that runs the rules as basis of logical inference.
- a **labeller** which actually labels the tissues.

A priori geometric knowledge

Geometrical information of the speciment localization can be retrieved by means an atlas; in fact, organ geometry can slightly differ from patient to patient. These differences could be found in localization, size or shape of the tissues. The comparison between patient images and atlases is possible only if both these volumes are defined in a common 3D-mesh. Since there weren't any atlases useful for this application, we built our own one. This a-priori geometric knowledge atlas (APGK) was created using the T2 image of the patients PRE scan by a multi-steps procedure (Figure 4.4), which consisted in 5 steps:

1. Re-sampling of the images histogram in a range between 0 and 1000 in order to make them conformable.
2. Registration of the patient images in a common 3D-mesh through a combination of rigid and non-rigid registrations.
3. Smoothing of all patient images.
4. Combining all these images using a mean operator, obtaining an average template.
5. Defining three areas on this atlas:
    - Region A: the area where penile bulb usually places;

- Region B: the area where we will search the bulb during the segmentation procedure;
- Region C: the area where there is a no-probability to find bulb.

In this way we identified region A as foreground and region B as background of APGK.
Once the images were rescaled in a range between [0 1000], we registered the morphological T2 images of every patients in a common 3D-mesh. Then a smoothing step was applied with σ=0.8. Afterwards, we combined smoothed T2 images with mean operator to have a unique sample image. In this volume, we identified the penile bulb (foreground) and a circular background area around the bulb with a ray of 5 cm in the 3D-direction. This last region could be used during the segmentation procedure in order to individuate the only area where search the bulb: so, we avoided false positives which arise from the presence of other tissues (such as the bladder) that have the same intensity values of the penile bulb.

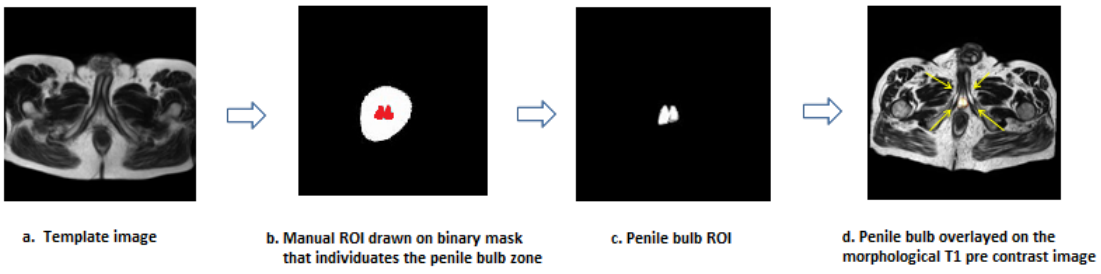

Figure 4.4: APGK of interest tissue used as sample image to localize and identify the penile bulb in the following steps.

Principal Component Analysis

Principal Component Analysis (PCA) is the most common used data reduction technique and is used to reduce the number of dimensions in a large number of variables. Data reduction techniques involve an investigation of the inter-relationships in a set number of variables. PCA finds a linear combination of m coordinates in order to express them in a new reference such that:

1. each principal component (PC) is a linear combination of the original variables;
2. the PCs are orthogonal and therefore mutually uncorrelated to each preceding other, suppressing redundant information;
3. to each eigenvector is associated an eigenvalue, which corresponds to the variance of the associated principal component. If the original variables are partially correlated, some eigenvalues will have a negligible values;

These new variables are derived in decreasing order of importance. If the dataset, at the beginning, is composed by m variables, then it can be had up m principal components. The first principal component accounts for the most larger variation in the original data. Thus, the PCA (Figure 4.5) provides an alternative explanation of the observed data variability. It provides the advantage of describing the phenomenon through dimensions unrelated to each other.

In this work, for each exam, PCA had as input the 8 images dataset and we calculated the linear combination for the maximization of the contrast data variance, defined as:

$$contrast\ variance\ data = \frac{ROI(foreground) - ROI(background)}{ROI(background)}$$

where the foreground is region A of APGK and the background is the region B of APGK. Thus, we obtained a set of directional cosines able to linearly combine all the images of the patients on a single space, which could amplify the difference of the background and foreground of the segmented image.

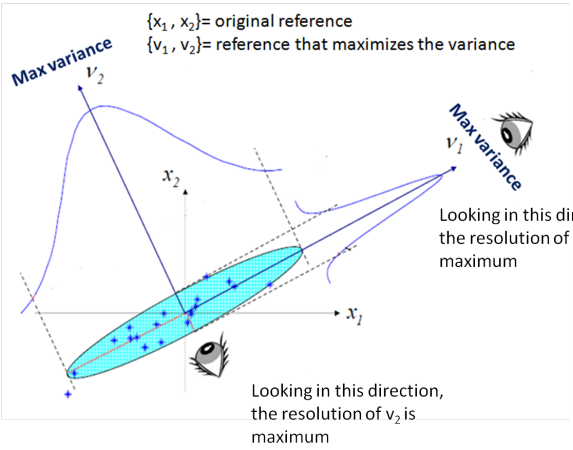

Figure 4.5: Principal Component Analysis creates a new variable set that contains the information from multiple, correlated, independent variables. This eliminates the issue of correlation while preserving the maximum amount of information.

Geometric model

The information retrieved by the region A of APGK was used to sample the bulb, in order to characterize quantitatively the tissue. The foreground of the APKG was used in this step to compute the distribution grey levels of the images (Figure 4.7).

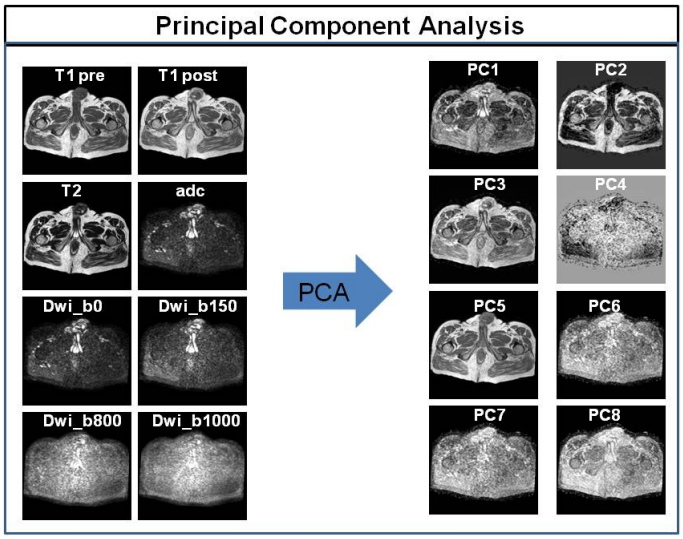

Figure 4.6: PCA dataset.

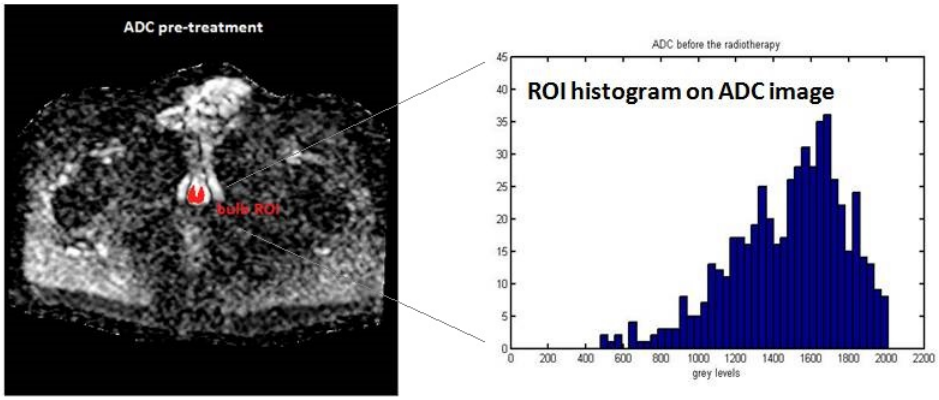

Figure 4.7: Geometric model creates grey levels histogram of the images.

Fuzzy sets creator

The grey levels histogram was used to define the probability of a voxel to represent the penile bulb. At this purpose, we implemented three different methods to generate the membership functions (MF) (Figure 4.8):

- Fuzzy multidimensional segmentation through Gaussian fitting of ROI histogram;
- Fuzzy multidimensional segmentation through ROI histogram;
- Segmentation through Multidimensional Threshold.

In the following paragraphs they are described more in detail.

Fuzzy multidimensional segmentation through Gaussian fitting of ROI histogram Grey levels histograms were then used to compute 8 membership functions (one for every techniques). We adopted a complex two-sided gaussian membership *gauss2mf* obtaining by a combination of two normalized gaussian function:

$$\begin{cases} f(x, \sigma_1, \mu_1) = e^{-\frac{(x-\mu_1)^2}{2\sigma_1^2}} \\ f(x, \sigma_2, \mu_2) = e^{-\frac{(x-\mu_2)^2}{2\sigma_2^2}} \end{cases}$$

where:

x is grey levels of the technique.

$\sigma_1 = \sigma_2$ and they are retrieved from standard deviation of the level distribution in the ROI.

μ_1 and μ_2 are two parameters which were calculated as:

$$\begin{cases} \mu_1 = \min(ROI) + 0.7 * \sigma_1 \\ \mu_2 = \max(ROI) - 0.7 * \sigma_2 \end{cases}$$

Particularly, the first function determines the shape of the leftmost curve while the second function determines the shape of the rightmost curve.

Fuzzy multidimensional segmentation through ROI histogram This second approach used the normalizing ROI histograms at 40 bin as membership functions. The histogram was defined as follows:

$$f(I_j(x,y,z)) = \frac{h_j^{ROI} I_j(x,y,z)}{max_k(h_j^{ROI}(k))} \tag{4.9}$$

where $h_j^{ROI}(k)$ is the number of voxels in the j-th image whose intensity value is k. The intensity value k varies in a continuous way along the intensity range with the same bin resolution of the original j-th image.

Segmentation through multidimensional threshold In this technique, a threshold value was chosen by the region A of APGK and the image is divided into groups of pixels that have values lower than the threshold and in groups of pixels with values greater or equal to it. For each registered image, the threshold algorithm established a criterion to decide whether a particular pixel should be included in the current region or not. The process of converting the grey levels of an image $f(i,j)$ in a binary image $g(i,j)$ is the simplest method of segmentation. A

value of grey level of separation between the two intervals was calculated in order to assign the value 1 to the pixels relating to objects and to assign the value 0 to the pixels relative to the background. If the range of the grey levels $[S_1, S_2]$ associated with the object is known, the binary image is obtained. Formally:

$$g(i,j) = \begin{cases} 0 & \text{if } S_1 \leq f(i,j) \leq S_2 \\ 1 & \text{otherwise} \end{cases}$$

where S_1 and S_2 are respectively the minimum and maximum of each image on which foreground APGK was applied.

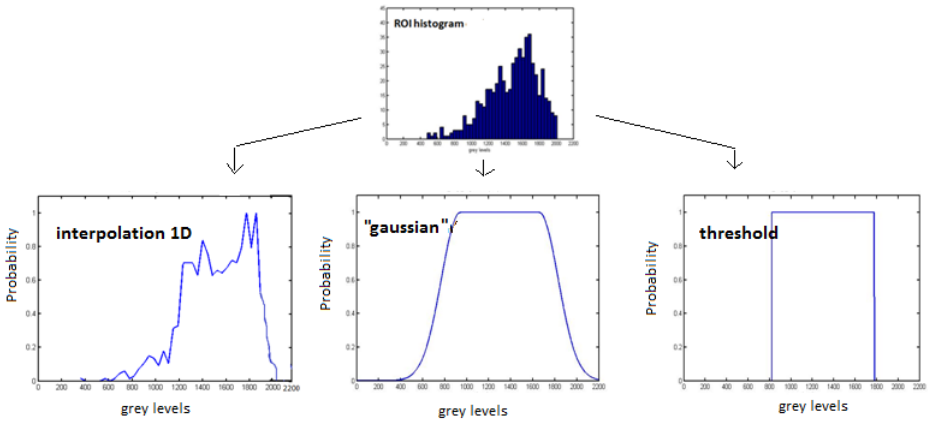

Figure 4.8: Fuzzy sets creator generates the different membership functions from the intensities' grey levels of the geometric model. Membership Functions were obtained through three different methods.

Intensity-based fuzzificator

Once membership functions were generated, we applied them as a look-up table to the images both pre and post-treatment exams.

Fuzzy inference engine

By applying the MFs to the input dataset, we obtained 16 probability maps, 8 in PRE and 8 in POST. For each scan, we computed a fuzzy conjunction operation by applying Mamdani minimum implication rules. At the end of this procedure we obtained 2 maps, one for each scan, measuring the probability of each voxel to be labelled as penile bulb.

Identification probability map and labelling

In the inference step, the contribute of each membership function was combined in order to obtain a probability map (Figure 4.9). This probability map was processed imposing a threshold value in order to obtain a binary image. We computed the optimal threshold performing a validation procedure [paragraph 4.3] Once the threshold was applied, the image was elaborated with *erosion* and *dilation* morphological operations in order to improve the segmentation. Matlab function *regionprops* allows to eliminate useless pixels having the same intensity but shape or size different from the bulb. We considered as final bulb ROI that blob having the maximum area individuated on the image and the minimum distance between the centroid of the blob on the segmented ROI and the other identified on the ROI made hand (Figure 4.9).

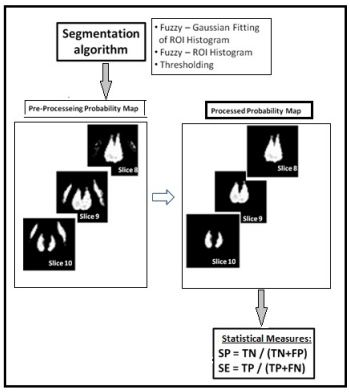

Figure 4.9: Identification of a probability map by means the application of a different membership functions (according to fuzzy sets creator chosen) and fuzzy Mamdani minimum implication rules. Image processing was computed on the final probability map to improve the segmentation.

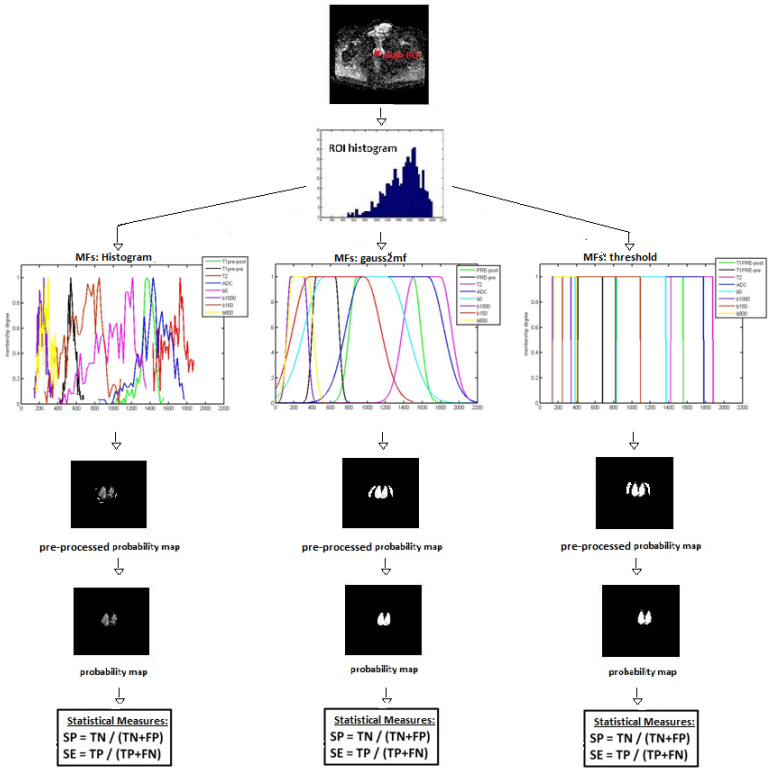

Figure 4.10: Identification of the penile bulb is the final result of an automatic segmentation procedure.

4.3 Validation of the segmentation procedure

In order to find the best combination of threshold and number of components, we set up a validation step. To verify the correct segmentation of the automatic procedure, we asked to the radiologist to drew a contour of the bulb. After that, by comparing of the hand made ROI with the output of the segmentation procedure (at the different components' number and threshold values), we could evaluate the accuracy of the entire algorithm. In this 3D-space (number of components, threshold value and percentage), we defined a metric to optimize both sensitivity and specificity of the technique:

$$metric = \frac{Specificity + Sensitivity}{2} \tag{4.10}$$

By maximizing this metric, we could find:

- the optimal fuzzy set creator [paragraph 4.2.1]
- threshold
- number of components.

4.3.1 Specificity and Sensitivity in the segmentation procedure

As explained in the previous section, we compared the hand made ROI with the output of the segmentation procedure. We considered the hand made ROI as the reference, while the output of the labeller

[paragraph 4.2.1] was the tested region. As reported in the figure 4.11, we defined four areas:

- Region A (True positive): is the area internal both in the hand made ROI and the segmentation output.
- Region B (False positive): is the area outside the hand made ROI but inside the segmentation output.
- Region C (False negative): is the area inside the hand made ROI but outside the segmentation output
- Region D (True negative): is the area external both in the hand made ROI and the segmentation output.

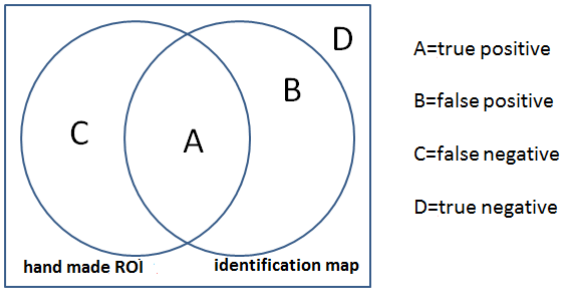

Figure 4.11: Validation of segmentation procedure.

4.3.2 Segmentation validation results

For each patient and each couple of values (the number of components and the segmentation threshold), we computed specificity and sensitivity [paragraph 3.3.1]: the average sensitivity and specificity were showed in the following box-plots and meshes (Figure 4.12, 4.13 and 4.14). Global data were collected for three implementation of the fuzzy set creator [paragraph 4.2.1]. We noticed that the little changes in the number of components used in the PCA or threshold result in a decrease of the sensibility and an increase of the specificity.

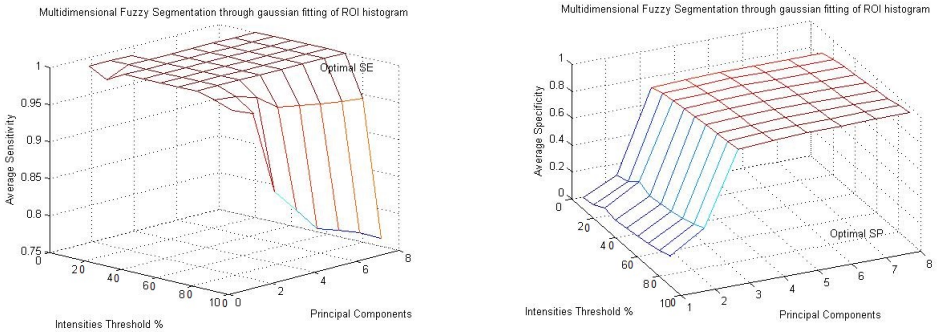

Figure 4.12: Sensitivity and specificity for the fuzzy segmentation through Gaussian fitting of ROI histogram.

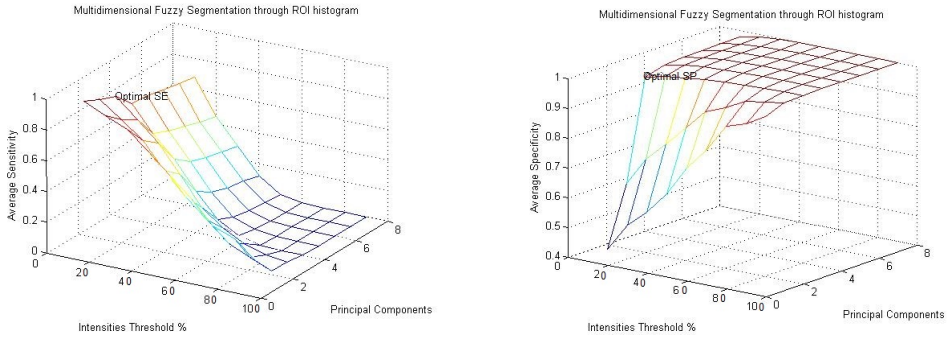

Figure 4.13: Sensitivity and specificity for the fuzzy segmentation through mono dimensional interpolation of ROI histogram.

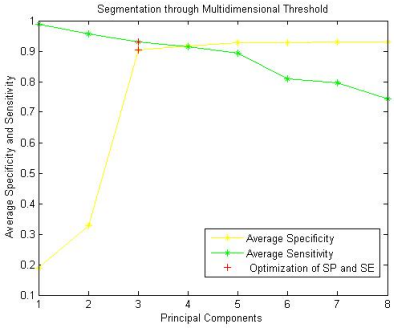

Figure 4.14: Sensitivity and specificity for the segmentation through thresholding.

We report in Tables 4.1 and 4.2 classification performances' values and the metric related to the optimal segmentation methods.

Table 4.1: The average values of sensitivity and specificity relating to the optimal segmentation methods.

Segmentation	**Princ. Comp.**	**Thresholds** (%)	**Specificity**	**Sensitivity**
Fitting gaussian	6	80	0.9350	0.9561
1-D interpolation	3	10	0.9541	0.8625
Thresholding	3	-	0.9030	0.9380

Table 4.2: The metric related to the optimal segmentation methods.

Segmentation	**metric**
Fitting gaussian	0.9455
1-D interpolation	0.9083
Thresholding	0.9205

4.4 Statistical tests on dose and ADC distributions

In order to evaluate the changes of ADC in the penile bulb we performed a statistical test using the Wilcoxon *rank-sum* test.
The Wilcoxon signed-rank test is a non-parametric statistical hypothesis test used when comparing two related samples, matched samples, or repeated measurements on a single sample to assess whether their population mean ranks differ. It can be used as an alternative to the paired Student's t-test, t-test for matched pairs, or the t-test for dependent samples when the population cannot be assumed to be normally distributed. This test returned the p_value of a two-sided Wilcoxon rank sum test, that proved the null hypothesis that data in x and y were independent samples from continuous distributions with equal medians, against the alternative that they were not. Low p_values cast doubt on the validity of the null hypothesis [18].
Therefore we tested the ADC distribution on pre and on post inside the bulb against the null hypothesis of no changes of two samples (Figure 4.3). We set the acceptance threshold at p=0.05.

Table 4.3: Wilcoxon rank sum test between ADC before and after radiotherapy treatment.

Patients	**p_value**	H_0 (p=0.05)
Pt1	1.0416 e^{-4}	refused H_0
Pt2	4.5736 e^{-14}	refused H_0
Pt3	3.1056 e^{-25}	refused H_0
Pt4	1.4248 e^{-36}	refused H_0
Pt5	0	refused H_0

Similarly, we used the Wilcoxon *rank-sum* test to evaluate the relationship between dose and ADC. The results obtained are reported in the following Table 4.4.

Table 4.4: Correlation between mean dose received and mean percentage variation of ADC within the penile bulb on the analysed population.

Patients	**mean dose**	**mean ΔADC**	**p_value**	**R**
Pt1	17.5364	0.0480	0.2220	-0.7780
Pt2	10.0665	0.0301	0.2431	0.7569
Pt3	38.3192	0.3468	0.0565	-0.9435
Pt4	5.4861	0.0673	-	-
Pt5	16.6668	0.2553	0.6296	0.5496

Chapter 5

Results

We divided the results of this thesis in three area: the registration results, the segmentation outcome and the studied relationship between ADC and dose.

Registration Results

Image registration is a key enabling technology in medical image analysis that has benefited from 20 years of development. As we explained, it is a process for determining the correspondence of features between images collected at different times or using different imaging modalities. Image registration is not an end in itself but adds value to images, for example by allowing structural (CT, MR, ultrasound) and functional (PET, SPECT, functional MRI (fMRI)) images to be viewed and analysed in the same coordinate system. Registration procedure also facilities new uses of images: it allows to monitor and quantify disease progression over time in the individual or to build statistical models of structural variation in a population. For all these motivations, we had to evaluate our registration method calculating its specificity and sensitivity. The test results are reported in Table 5.1.

Table 5.1: Sensitivity and specificity of the registration procedure.

Registrations	**Sensitivity**	**Specificity**
Intra-exam registration	0.987	0.992
Inter-exam registration	0.923	0.998
Ct inter-exam registration	0.997	0.998

The specificity and the sensitivity median values were greater than 0.9 (maximum is equal to 1). It means that the error committed is not high and the fixed ROI and the registered one overlap with a good accuracy. This results allowed us to directly compare the images in the following steps of the study.

Segmentation results

Once the metric was quantified, we choose the best implemented segmentation method: the segmentation through Gaussian fitting of the ROI histogram with threshold = 80% and 6 principal components were selected. We reported in Table 5.2 the value of the sensitivity e specificity for each patient.

Table 5.2: Final validation - the sensitivity and specificity relating to the Gaussian fitting at 6 PCs and threshold 80%.

Patients	**Specificity**	**Sensitivity**
Pt1	0.9730	0.9702
Pt2	0.8694	0.9186
Pt3	0.8909	0.9457
Pt4	0.9875	0.9769
Pt5	0.9381	0.9623

We obtained high values of the classification performances, which were considered acceptable also after a qualitative evaluation by the radiologist.

ADC-Dose relation results

We portrayed the ADC values within the region of interest (the penile bulb) in Figure 5.1. Each box plots corresponds to a patient.

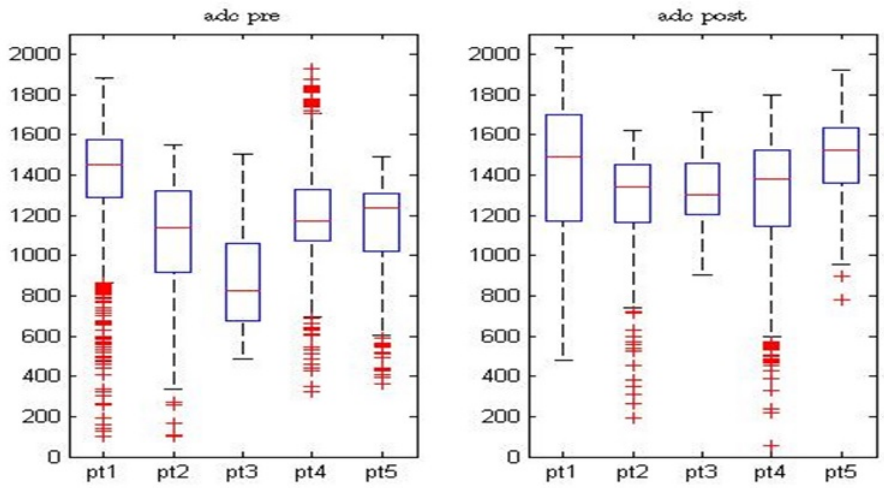

Figure 5.1: ADC values calculated before (on the left) and after (on the right) the radiotherapy treatment: the increase of the ADC values from the pre to the post treatment examination is very obvious to all patients.

The overall effect on the population was that ADC rose in the short period after the radiotherapy, although for some patients in a more evident way than in others. We noticed a greater increase in both the third and fifth patient. In order to testify the statistical significance of the differences between ADC pre and post treatment, we used Wilcoxon *rank-sum* [paragraph 4.4] test.

Table 5.3: Wilcoxon rank sum test between ADC before and after radiotherapy treatment.

Patients	**p_value**	H_0 (p=0.05)
Pt1	1.0416 e^{-4}	refused H_0
Pt2	4.5736 e^{-14}	refused H_0
Pt3	3.1056 e^{-25}	refused H_0
Pt4	1.4248 e^{-36}	refused H_0
Pt5	0	refused H_0

By the results of the test, we could refuse the null hypothesis of no effect of the radiotherapy (Table 5.3). In order to make the patients comparable, we normalized the ADC variation [10] as follows:

$$normalized\ ADC\ values = \frac{post\ treatment\ ADC - pre\ treatment\ ADC}{pre\ treatment\ ADC} \tag{5.1}$$

Positive values mean an increase of the post-treatment ADC compared to the pre-treatment one, while negative values were the other way around. Then we represented the mean ADC and dose values for each patient, as shown in figure 5.2. We observed small variations in ΔADC values for the ranges of dose considered.

The low linear correlation between dose and the percentage variation of the ADC is also demonstrated by the calculation of the p_ value in Table 5.4. The values were greater than 0.05 over the whole sample.

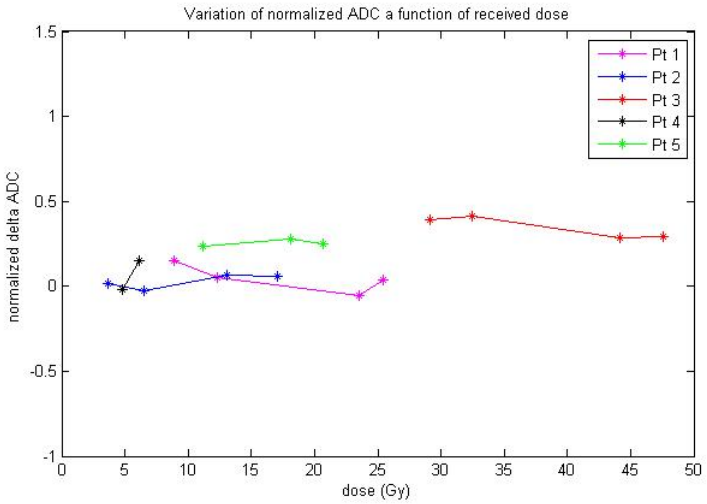

Figure 5.2: The percentage variation of the ADC is almost constant within penile bulb for the range of dose at which patients were exposed.

Table 5.4: Correlation between mean dose received and mean percentage variation of ADC within the penile bulb on the analysed population.

Patients	**mean dose**	**mean ΔADC**	**p_value**	**R**
Pt1	17.5364	0.0480	0.2220	-0.7780
Pt2	10.0665	0.0301	0.2431	0.7569
Pt3	38.3192	0.3468	0.0565	-0.9435
Pt4	5.4861	0.0673	-	-
Pt5	16.6668	0.2553	0.6296	0.5496

Three patients had an increase of ADC between 0% and 6%, instead for the others two the enhancement was of 35% and 25%. The results showed that a low ADC growth was not in every case justifiable with a low quantity of dose. In fact, for a comparable quantities of dose received, we found different ADC increases. In order to find other elements related with the changes in ADC, we examined the International Index of Erectile Functionality questionnaires (IIEF).

A score between 0 and 30 quantify the erectile functionality:

- a score between 1 and 10 indices severe dysfunction.
- a score between 11 and 16 indices moderate dysfunction.
- a score between 17 and 25 indices mild dysfunction.
- a score between 26 and 30 indices absence dysfunction.

We resumed all information obtained in our work in Table 5.5.

Table 5.5: Information acquired on the analysed population.

Patients	**Age (years)**	**Mean ΔADC**	**Median ΔADC**	**IIEF**
Pt1	75	0.1049	0.0635	16
Pt2	73	0.0326	0.0201	16
Pt3	65	0.4319	0.4451	21
Pt4	72	0.1719	0.1929	23
Pt5	64	0.2797	0.2366	30

Patients were classified into two groups according to the degree of erectile dysfunction: the first group included individuals with a moderate or severe erectile dysfunction (patients 1 and 2); the second one consist of the patients, who had a mild or no erectile dysfunction (patients 3, 4 and 5). Thus, we compared the mean and median ADC value with the IIEF score. As reported in Figure 5.3, the averages for the first group were lower than the values of the second one. The same result was found for the median ADC values.

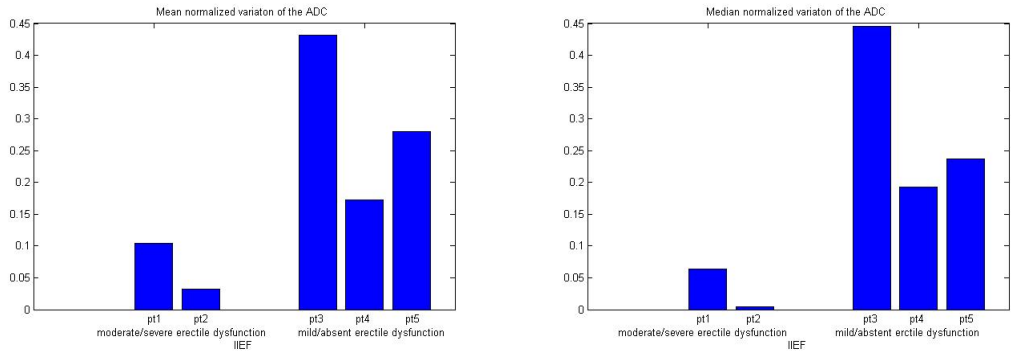

Figure 5.3: The outcome of the IIEF questionnaires in function of the mean or median calculated for normalized variation ADC of each patient.

Chapter 6

Conclusion and future developments

There are a number of studies in literature regarding the characterization of tumour tissues and diseases evaluation in both the short (within 3 months) and long term period (up to 24 months) after the radiotherapy. These researches are based mainly on parameters of the tissue perfusion and cellularity. Despite that, there are few studies concerning with the evaluation of the only response to radiotherapy treatment of healthy tissue included in the PTV. However, none have been found on the functional assessment of the penile bulb like as an healthy tissue marginally affected by radiations. Therefore the aim of this work is to assess the effects of radiation at the cellular level on healthy tissues, in particular on penile bulb.

Despite the results obtained in this study are preliminary, we can conclude that magnetic resonance diffusion-weighted imaging may potentially be a valuable tool to predict radiosensitivity. We considered the ADC as a parameter of tissue cellularity, useful to assess the treatment response of the penile bulb. In particular for all patients ADC increase within three months after the start of the radiotherapy treatment.

Statistical tests, which have been performed on this parameter within the bulb, show that the differences might be considered statistically significant. This results are in line with the literature (Larocque and al [23]). They observed for treated groups a common behaviour, which depended not only the value of the ADC but also on the radiation dose. In particular, ADC was sensitive to radiation-induced changes in lower dose groups. This is different with the results from the current study, which did not show any significant correlation between changes in ADC and the dose received by the single patient.

In order to justify the different increase of ADC between the patients, for an equal level of dose, we supposed the existence of an individual radiosensitivity. This theory is confirmed by another study of Larocque and his team [24]: their results affirmed that the response of the ADC to the radiation therapy is not determined entirely by physical dose deposition, but, at least in part, by the radiosensitivity and the resultant biological response.

Furthermore we have found a relationship between percentage variation in the ADC and the erectile dysfunction.

In particular, it has been observed that patients which have an higher increase of ADC are the same who presented a lower erectile dysfunction. This result is opposite of the one that could have been expected. This fact could mean that there is not a relationship between the dysfunction and the dose received, but there are other elements that influenced the dysfunction such as age or comorbidity [1].

[1] The comorbidity terms refers to the simultaneous presence in the same person more diseases that between them show no causal link: that could be linked also to the taking medications or lifestyle (alcohol, smoking).

In the literature few are the available informations on the erectile dysfunction (ED) or toxicity genitourinary (GU), especially the data on the correlation between clinical-dosimetry risk factors and toxicity ED/GU are scarce and contradictory. Synthetic and analytical scores that describe the toxicity will be derived from questionnaires administered by the patients.

Merrick [30] evaluated whether radiation doses to the bulb of the penis and/or the proximal corporeal bodies were predictive for the development of the brachytherapy-induced ED. They discovered that the radiation dose delivered to the bulb of the penis and the proximal crura in men with brachytherapy-induced ED was statistically greater that in men without ED. Moreover, also patient age at implantation time was predictive of postimplant-ED.

Taussky and his team [40] arrived at the same conclusion: they used Spearman's correlation to establish a relation between dosimetric parameters, anatomical factors and the dose to the penile bulb. About one-third of the patients received a dose to the bulb, that would put them at a high risk of erectile dysfunction after external beam radiation. Instead, a correlation between the dose to the prostate (or its apex) and the dose to the penile bulb could not be identified. Despite of that, when the prostate apex is close to the penile bulb, it is required to carefully operate to limit the dose to the penile bulb, because this may reduce the incidence of erectile dysfunction and urinary toxicity.

Contrariwise, Solan [39] affirmed that there is no correlation between dose to penile bulb and the development of post-implantation impotency and this is in accord with our results. One hundred forty-seven patients was undergone prostate brachytherapy with a prescribed dose

of 160 Gy, who were defined as potent before the time of implantation and they had a minimum follow-up of 12 months. The 3-year actuarial rate of impotence was 23% (34 of 147 patients). An additional 43% of potent patients (49 of 113 patients) were using a potency aid at last follow-up.

Therefore, it is difficult to establish a unique and significant relationship between literature data and the results obtained. The small number of patients recruited also does not allow to give a definitive and unambiguous answer about the functional assessment of the penile bulb. The great variability in the results makes it impossible to draw firm conclusions. Despite of that, this work suggest an accurate registration method and a good segmentation algorithm. Moreover, drown attention to the proven radiosensitivity problem. Discover the characteristics that are closely related with the subjective radiosensitivity, can help the clinicians to plan a specific radiotherapy treatment. Through a larger sample would be possible to re-check as shown and find elements that bind those who belong to the group of "radiosensitive". This study shows how a Magnetic Resonance examination dataset with different contrast images could collect many information not only about the disease evaluation but also functional evaluation of the healthy tissues in those patient affected from prostate cancer. Furthermore, there are many advantages in using MRI: first patient does not suffer ionizing radiation exposure, second the whole examination is taken in the same place, and finally the MRI is more efficient than other techniques as costs are lower and results on higher resolution images.

Appendix A

MR basic sequences

Generally for weighted images it is used a set of RF pulses applied to a sample to produce a specific form of MR signal. Among these the most common pulse sequences are:

- **SR** (Saturation Recovery) is the simplest sequence, consists of a 90°pulse repeated in time. Net magnetization is rotated down into the xy plane with a 90 pulse. The net magnetization vector $M_{xy} = M_0$ begins to precess about the z axis and decays with time. When this sequence is repeated, for example when signal-to-noise improvement is needed, the amplitude of the signal after being Fourier transformed (S) will depend on the time between repetitions, called the repetition time (T_R), ρ and T1 (if $T_R >$ T2 and $\approx$ T1), of the sequence.

$$\mathrm{S} = \mathrm{k}\rho(1 - e^{\frac{-T_R}{T1}}) \tag{A.1}$$

  It is noted also that if $T_R \gg T1$, the signal is only dependent on T_R and ρ, that is the density of spins in the sample.

- **IR** (Inversion Recovery) sequence is constituted by a 180°-impulse followed by an 90° impulse, applied after a time T_i. The first impulse doesn't emit a useful signal since magnetization M_{xy}, changing verse but maintaining parallel to magnetic field B_0, results zero. After this impulse, the magnetization along z axis M_z try to reach the balance with M_z=-M_0 and time constant T1. At T_i time, magnetization along principal axis is turned until the precession movement will begin in the transversal plane. After T_i<T1, the spin realignment along the z axis happens, so the effect of 90°impulse generates a signal proportional to:

$$\mathrm{S} = \mathrm{k}\rho(1 - 2e^{\frac{-T_i}{T1}}) \tag{A.2}$$

If identical and second sequence is applied after T_R, the amplitude of the second FID, that depends on T1 and ρ, results as:

$$\mathrm{S} = \mathrm{k}\rho[(1 - e^{\frac{-T_i}{T1}} + e^{\frac{-T_R}{T1}})] \tag{A.3}$$

- **SE** (Spin Echo) sequence consists of a 90° pulse followed by a 180 ° pulse after a time interval $\frac{T_E}{2}$. The 90° pulse effect at t=0 consists in: $M_{xy} = M_0$ and $M_z = 0$. After a time interval $\frac{T_E}{2}$, the transversal magnetization M_{xy} is vanished for the spin dephasing effect due to the field inhomogeneity. The effect of a

180° pulse in $\frac{T_E}{2}$ is to flip the spins over the other side of the xy plane: gradual recover of spins phase coherence. Since each spin is immersed in the same magnetic field earlier, it "come back" with the same speed as before, causing a "rewind" of the phases and a reacquisition of coherence from the signal. In TE, spins are again in phase and an echo signal can be measured. The echo amplitude is proportional to $\rho\ e^{\frac{-T_E}{T2}}$ However, the maximum amplitude will be less than the amplitude of the FID previously recorded, as in the meantime the spins will have received a T2 decay. If a second identical sequence is applied after a repetition time $T_R \gg T_E$ (with $T_E \geq T2$), the amplitude of the signal is proportional to:

$$\mathrm{S} = \mathrm{k}\rho((1 - e^{\frac{-T_R}{T1}})\ e^{\frac{-T_E}{T2}}). \tag{A.4}$$

The signal equation for a repeated spin-echo sequence as a function of the repetition time T_R and the echo time T_E. It is also possible to verify that for $T_R \gg T1$ and $T_E \gg T2$ proton density images are obtained; analogously, for $T_R \approx T1$ and $T_E \ll T2$ T1 weighted images are got.

List of abbreviation

ADC Apparent Diffusion Coefficient

APGK A-Priori Geometric Knowledge

CT Computed Tomography

DF Deformation Field

DWI Diffusion Weight Image

IIEF International Index of Erectile Functionality

IRTK Image registration Toolkit

ITK Inside Segmentation and Registration Toolkit

MF Membership Function

MRI Magnetic Resonance Image

PCA Principal Component Analysis

POST morphological T1 post-treatment image

PRE morphological T1 pre-treatment image

PTV Planning Target Volume

ROI Region of Interest

RT Radiotherapy

Bibliography

[1] H. Aydin, V. Kizilgoz, I. G. Tatar, C. Damar, A. R. Ugan, I. Paker, and B. Hekimo?lu. Detection of prostate cancer with magnetic resonance imaging: optimization of T1-weighted, T2-weighted, dynamic-enhanced T1-weighted, diffusion-weighted imaging apparent diffusion coefficient mapping sequences and MR spectroscopy, correlated with biopsy and histopathological findings. *J Comput Assist Tomogr*, 36(1):30–45, 2012.

[2] B. Babourina-Brooks, G. J. Cowin, and D. Wang. Diffusion-weighted imaging in the prostate: an apparent diffusion coefficient comparison of half-Fourier acquisition single-shot turbo spin-echo and echo planar imaging. *Magn Reson Imaging*, 30(2):189–194, Feb 2012.

[3] M. K. Bucci, A. Bevan, and M. Roach. Advances in radiation therapy: conventional to 3D, to IMRT, to 4D, and beyond. *CA Cancer J Clin*, 55(2):117–134, 2005.

[4] J. H. Burdette, A. D. Elster, and P. E. Ricci. Calculation of apparent diffusion coefficients (ADCs) in brain using two-point and six-point methods. *J Comput Assist Tomogr*, 22(5):792–794, 1998.

[5] RH Byrd, Jorge Nocedal, and RB Schnabel. Representations of quasi-Newton matrices and their use in limited memory methods. *Math. Program.*, 63(2):129–156, 1994.

[6] C. Introini C. E. Neumaier P. Puppo F. Ricci B. Spina L. Tomasello F. Boccardo, S. Barra. Carcinoma della prostata. 2010.

[7] T. Franiel, N. Eckardt, M. Waginger, and M. Horstmann. [Prostate cancer.]. *Radiologe*, Feb 2014.

[8] J. M. Galvin, G. Ezzell, A. Eisbrauch, C. Yu, B. Butler, Y. Xiao, I. Rosen, J. Rosenman, M. Sharpe, L. Xing, P. Xia, T. Lomax, D. A. Low, and J. Palta. Implementing

IMRT in clinical practice: a joint document of the American Society for Therapeutic Radiology and Oncology and the American Association of Physicists in Medicine. *Int. J. Radiat. Oncol. Biol. Phys.*, 58(5):1616–1634, Apr 2004.

[9] Sujit Nath Pant Keith E. Holbert. *Fuzzy Logic in Decision Making and Signal Processing*. 2004.

[10] J. Hong, Y. Yao, Y. Zhang, T. Tang, H. Zhang, D. Bao, Y. Chen, and J. Pan. Value of magnetic resonance diffusion weighted imaging for the prediction of radiosensitivity in nasopharyngeal carcinoma. *Otolaryngol Head Neck Surg*, 149(5):707–713, Nov 2013.

[11] http://en.wikipedia.org/wiki/External_beam_radiation_therapy.

[12] http://en.wikipedia.org/wiki/Radiation_therapy.

[13] http://it.wikipedia.org/wiki/Imaging_a_risonanza_magnetica.

[14] http://plastimatch.org/registration_command_le_reference.html.

[15] http://www.cabiatl.com/mricro/mricro/mricro/mricro.html.

[16] http://www.doc.ic.ac.uk/dr/software/index.html.

[17] http://www.emedicine.medscape.com.

[18] http://www.mathworks.com.

[19] http://www.mayoclinic.org/diseases_conditions/prostate_cancer/basics/definition.

[20] http://www.prostatecancer.com/prostate_cancer_treatment_overview.html.

[21] L.G. Salvador J.G. Cabada. *Fuzzy System for Intelligent Automatic Door's Opening Control*. Dpto. Ingenieria Software e Inteligencia Artificial. Facultad de Informatica, Universidad Complutense de Madrid, 28040-Madrid, Spain.

[22] Ph.D. Joseph P. Hornak. *The basic of MRI*. Interactive Learning Software, 2008.

[23] M. P. Larocque, A. Syme, J. Allalunis-Turner, and B. G. Fallone. ADC response to radiation therapy correlates with induced changes in radiosensitivity. *Med Phys*, 37(7):3855–3861, Jul 2010.

[24] M. P. Larocque, A. Syme, A. Yahya, K. Wachowicz, J. Allalunis-Turner, and B. G. Fallone. Monitoring T2 and ADC at 9.4 T following fractionated external beam radiation therapy in a mouse model. *Phys Med Biol*, 55(5):1381–1393, Mar 2010.

[25] K. H. Leissner and L. E. Tisell. The weight of the human prostate. *Scand. J. Urol. Nephrol.*, 13(2):137–142, 1979.

[26] M. F. Leitzmann, E. A. Platz, M. J. Stampfer, W. C. Willett, and E. Giovannucci. Ejaculation frequency and subsequent risk of prostate cancer. *JAMA*, 291(13):1578–1586, Apr 2004.

[27] Zhi-Pei Liang and Paul C Lauterbur. Principles of magnetic resonance imaging: a signal processing perspective. *SPIE Optical Engineering Press New York*, 2000.

[28] X. Liu, W. Peng, L. Zhou, and H. Wang. Biexponential apparent diffusion coefficients values in the prostate: comparison among normal tissue, prostate cancer, benign prostatic hyperplasia and prostatitis. *Korean J Radiol*, 14(2):222–232, 2013.

[29] S. Lutz, L. Berk, E. Chang, E. Chow, C. Hahn, P. Hoskin, D. Howell, A. Konski, L. Kachnic, S. Lo, A. Sahgal, L. Silverman, C. von Gunten, E. Mendel, A. Vassil, D. W. Bruner, and W. Hartsell. Palliative radiotherapy for bone metastases: an ASTRO evidence-based guideline. *Int. J. Radiat. Oncol. Biol. Phys.*, 79(4):965–976, Mar 2011.

[30] G. S. Merrick, W. M. Butler, K. E. Wallner, J. H. Lief, R. L. Anderson, B. J. Smeiles, R. W. Galbreath, and M. L. Benson. The importance of radiation doses to the penile bulb vs. crura in the development of postbrachytherapy erectile dysfunction. *Int. J. Radiat. Oncol. Biol. Phys.*, 54(4):1055–1062, Nov 2002.

[31] D. C. Miller, K. S. Hafez, A. Stewart, J. E. Montie, and J. T. Wei. Prostate carcinoma presentation, diagnosis, and staging: an update form the National Cancer Data Base. *Cancer*, 98(6):1169–1178, Sep 2003.

[32] Messina A. Montin E. and Mainardi L. A full automatic method for the soft tissues sarcoma treatment response based on fuzzy logic. 2013.

[33] R. P. Myers. Structure of the adult prostate from a clinician's standpoint. *Clin Anat*, 13(3):214–215, 2000.

[34] Y. Peng, Y. Jiang, T. Antic, I. Sethi, C. Schmid-Tannwald, S. Eggener, and A. Oto. Apparent diffusion coefficient for prostate cancer imaging: impact of B values. *AJR Am J Roentgenol*, 202(3):W247–253, Mar 2014.

[35] B. Raychaudhuri and D. Cahill. Pelvic fasciae in urology. *Ann R Coll Surg Engl*, 90(8):633–637, Nov 2008.

[36] Cates J. Schroeder W., Ng L. *The ITK Software Guide Updated for ITK version 2.4*. the Insight Software Consortium, second edition, November 2005.

[37] J A Shackleford, N Kandasamy, and G C Sharp. {O}n developing {B}-spline registration algorithms for multi-core processors. *Phys Med Biol*, 55(21):6329–6351, November 2010.

[38] R. Siegel, E. Ward, O. Brawley, and A. Jemal. Cancer statistics, 2011: the impact of eliminating socioeconomic and racial disparities on premature cancer deaths. *CA Cancer J Clin*, 61(4):212–236, 2011.

[39] A. N. Solan, J. A. Cesaretti, N. N. Stone, and R. G. Stock. There is no correlation between erectile dysfunction and dose to penile bulb and neurovascular bundles following real-time low-dose-rate prostate brachytherapy. *Int. J. Radiat. Oncol. Biol. Phys.*, 73(5):1468–1474, Apr 2009.

[40] D. Taussky, M. Haider, M. McLean, I. Yeung, T. Williams, S. Pearson, G. Lockwood, and J. Crook. Factors predicting an increased dose to the penile bulb in permanent seed prostate brachytherapy. *Brachytherapy*, 3(3):125–129, 2004.

[41] C. M. Yashar, S. Blair, A. Wallace, and D. Scanderbeg. Initial clinical experience with the Strut-Adjusted Volume Implant brachytherapy applicator for accelerated partial breast irradiation. *Brachytherapy*, 8(4):367–372, 2009.

[42] Terry S Yoo. Insight into images.

[43] T. Yoshizako, A. Wada, K. Uchida, S. Hara, M. Igawa, H. Kitagaki, and S. E. Maier. Apparent diffusion coefficient of line scan diffusion image in normal prostate and prostate cancer–comparison with single-shot echo planner image. *Magn Reson Imaging*, 29(1):106–110, Jan 2011.